



FRET and optical trapping reveal mechanisms of actin activation of the power stroke and phosphate release in myosin V

Received for publication, August 15, 2020, and in revised form, October 6, 2020. Published, Papers in Press, October 14, 2020, DOI 10.1074/jbc.RA120.015632

Laura K. Gunther¹, John A. Rohde², Wanjian Tang¹ , Joseph A. Cirilo, Jr.¹, Christopher P. Marang³, Brent D. Scott³, David D. Thomas², Edward P. Debold³, and Christopher M. Yengo^{1,*}

From the ¹Department of Cellular and Molecular Physiology, Pennsylvania State College of Medicine, Hershey, Pennsylvania, USA, the ²Department of Biochemistry, Molecular Biology, and Biophysics, University of Minnesota Twin Cities, Minneapolis, Minnesota, USA, and the ³Department of Kinesiology, University of Massachusetts, Amherst, Massachusetts, USA

Edited by Enrique M. De La Cruz

Myosins generate force and motion by precisely coordinating their mechanical and chemical cycles, but the nature and timing of this coordination remains controversial. We utilized a FRET approach to examine the kinetics of structural changes in the force-generating lever arm in myosin V. We directly compared the FRET results with single-molecule mechanical events examined by optical trapping. We introduced a mutation (S217A) in the conserved switch I region of the active site to examine how myosin couples structural changes in the actin- and nucleotide-binding regions with force generation. Specifically, S217A enhanced the maximum rate of lever arm priming (recovery stroke) while slowing ATP hydrolysis, demonstrating that it uncouples these two steps. We determined that the mutation dramatically slows both actin-induced rotation of the lever arm (power stroke) and phosphate release (≥ 10 -fold), whereas our simulations suggest that the maximum rate of both steps is unchanged by the mutation. Time-resolved FRET revealed that the structure of the pre- and post-power stroke conformations and mole fractions of these conformations were not altered by the mutation. Optical trapping results demonstrated that S217A does not dramatically alter unitary displacements or slow the working stroke rate constant, consistent with the mutation disrupting an actin-induced conformational change prior to the power stroke. We propose that communication between the actin- and nucleotide-binding regions of myosin assures a proper actin-binding interface and active site have formed before producing a power stroke. Variability in this coupling is likely crucial for mediating motor-based functions such as muscle contraction and intracellular transport.

Understanding how motor proteins such as myosin couple structural changes in their ATPase cycle with mechanical force is a fundamental question in biophysics. Indeed, the actomyosin ATPase mechanism is utilized for many different mechanical tasks in cells including muscle contraction, cell division, and organelle transport (1). The large family of myosins, which includes over 20 classes and more than 40 different human genes, is defined by a structurally conserved motor domain and uses a conserved ATPase cycle to convert chemical energy

from ATP hydrolysis into mechanical work (2–4). A detailed understanding of the structural and functional aspects of the myosin ATPase pathway will enhance our ability to utilize myosins as drug targets to treat various genetic and pathological diseases (5).

The lever arm hypothesis suggests that myosins generate force by coupling specific conformational changes in the active site to large conformational changes in the actin-binding and lever arm regions (4, 6–8). The lever arm domain consists of a single α -helix that extends from the motor and binds a variety of calmodulin or calmodulin-like light chains. When myosin is bound to actin, its cytoskeletal track, the rotation of the lever arm can produce a power stroke that drives actin filament sliding or allows myosin to walk along actin filaments. A key question in the field is how does actin binding trigger the dramatic acceleration in the release of the products of ATP hydrolysis, specifically phosphate release, which can be accelerated over 1000-fold (9, 10), and how this is coupled to force production (*i.e.* lever arm rotation when myosin is bound to its track). There have been many approaches to addressing this question, including X-ray crystallography (4), solution biochemical analysis (10), single-molecule mechanical studies (11–13), and muscle mechanics studies (14, 15).

The challenge is to integrate all of the results in the literature into a model that describes the sequence of events associated with actin-binding, lever arm rotation (referred to as the power stroke), and force generation (referred to as the working stroke). Structural studies have defined two main conformations of the lever arm, the pre-power stroke state, in which ATP or the products of ATP hydrolysis are tightly bound to the active site, and a post-power stroke state, in which ADP or no nucleotide is bound (16). Crystallography results on myosin VI have provided insight into the phosphate release mechanism by demonstrating evidence of the escape route of phosphate through a phosphate tunnel or back door (17). Based on the crystallography studies, as well as other results in the literature, this group proposed that myosin binding to actin triggers structural changes in the active site that allow phosphate to be released through the back door. They propose that once phosphate is transitioned from the active site into the tunnel, strong actin binding and lever arm swing can occur and then finally phosphate leaves the tunnel into solution (4). Therefore, in this

This article contains supporting information.

* For correspondence: Christopher M. Yengo, cm11@psu.edu.

model, only when myosin is tightly bound to its track does it trigger the movement of the force-generating lever arm and allow the release of phosphate, a highly irreversible step in the absence of load. Consequently, studies that have directly measured the lever arm rotation by FRET in real time demonstrated that the power stroke occurs before the release of phosphate is observed (18–20). In addition, recent ultra-fast optical trapping studies on myosin II suggest that the power stroke and observed working stroke occur rapidly after attachment to actin, without any delay that might be caused by an intermediate with phosphate in the tunnel (21). Both models suggest that the power stroke and strong actin binding are tightly coupled. There are several key questions that remain to test current models. Foremost is defining structural changes in the active site that are triggered by attachment to actin and required for the power stroke and phosphate release. Carefully chosen point mutations designed to inhibit the lever arm rotation or phosphate release could provide a powerful test of these models. It is also unclear whether all myosins follow the same sequence of events or whether there are variations within the myosin family that are important for tuning myosins for their biological function.

We have developed a method of measuring the rotation of the lever arm in myosin V in real time using FRET, which involves labeling myosin V containing a single IQ motif with FAsH at its N terminus and exchanging QSY-labeled calmodulin at the first IQ motif (18). We directly measured lever arm rotation in the recovery and power stroke steps of the myosin V ATPase cycle and found that the power stroke occurs in two steps: a rapid step that is faster than phosphate release and a slower step that occurs before ADP release (18, 22). In the current paper we use a point mutation in the conserved switch I region of the active site to demonstrate the coupling between the actin- and nucleotide-binding regions during the power stroke and phosphate release steps. We also characterized the impact of the mutation in single-molecule mechanics and kinetics in an optical trapping assay. Our results have led to a model suggesting that the transition from a weak-binding state to an initial force-bearing state requires structural changes in the active site and that these actin-induced structural changes are crucial for triggering the power stroke. Thus, generating the myosin power stroke requires priming the key structural elements for force generation; actin-binding region, active site, and lever arm.

Results

S217A mutation in myosin V

The switch I region of the active site, which shares homology with other P-loop ATPases including kinesin and G-proteins, consists of a consensus motif (NXXSSR) (Fig. 1A) (23). Mutating the first serine in this motif was found to reduce but not abolish actin-activated ATPase and *in vitro* motility in myosin II (24, 25). Another study examined the impact of mutating this residue (S217A) in myosin V using steady-state and transient kinetic analysis as well as single-molecule motility (26), but optical trapping and structural kinetics were not examined. Thus, we introduced the S217A point mutation into a construct of

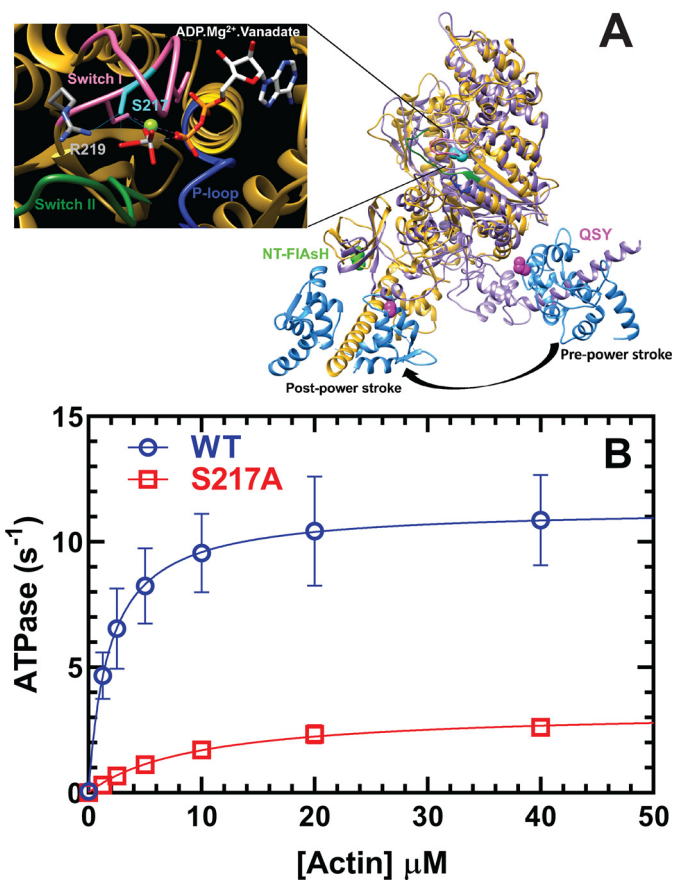


Figure 1. Actin-activated ATPase activity of S217A. A, the S217A mutation is located in switch I, a conserved region of the active site (see close-up of active site). The location of the fluorescent probes used for monitoring lever arm rotation are also highlighted with the lever arm in the pre- (Protein Data Bank entry IVOM) and post-power stroke (Protein Data Bank entry 1OE9) positions. The N-terminal FAsH label served as a donor for QSY labeled at T110C of calmodulin bound to the first IQ motif of myosin V (structural model was generated using *Chimera*). B, actin-activated ATPase was monitored as a function of actin concentration, and data were fit to Michaelis-Menten kinetics (summarized in Table 1). Error bars represent the standard deviation from at least three separate protein preparations.

myosin V contained a single IQ motif (MV), N-terminal tetracysteine tag, and C-terminal Myc and FLAG tags (18, 22, 27–29). For experiments utilizing FRET to measure lever arm rotation, we labeled MV with the tetracysteine-based dye FAsH and exchanged QSY-CaM onto the first IQ motif (MV-F.QSY-CaM) (Fig. 1A) (18, 22). The measurements not involving FRET were done with unlabeled WT and S217A in KMg50 buffer (10 mM imidazole, 50 mM KCl, 1 mM MgCl₂, 1 mM EGTA, and 1 mM DTT), whereas the FRET measurements were performed with MV-F.QSY-CaM in KMg50 buffer with 1 mM TCEP instead of DTT. In our previous work we demonstrated that our fluorescence labeling strategy had a slight impact on steady-state ATPase and *in vitro* motility (<2-fold) because of a reduction in the ADP release rate constant, whereas other steps in the ATPase cycle were unchanged (18).

Steady-state motor properties

We examined S217A compared with WT using actin-activated ATPase assays in KMg50 buffer at 25 °C (Fig. 1B) (18, 22). S217A reduced the maximum rate of actin-activated ATPase (k_{cat}) 3–4-

Table 1
 Summary of steady-state and transient kinetic results

	WT	S217A
Steady-state ATPase values (\pmS.E.), $n = 4^a$		
v_0 (s^{-1})	0.05 ± 0.06	0.01 ± 0.01
k_{cat} (s^{-1})	11.3 ± 0.6	3.3 ± 0.5^b
K_{ATPase} (μ M)	1.8 ± 0.4	9.6 ± 1.5^b
Rate/equilibrium constants (\pmS.E.)		
ATP binding/hydrolysis (myosin), $n = 3^c$		
$K_{1T}k_{+2T}$ (μ M $^{-1}$ · s^{-1})	1.8 ± 0.3	2.9 ± 0.9
$K_{0.5}$ (μ M)	196 ± 45	3.2 ± 1.3^d
$k_{+H} + k_{-H}$ (maximum rate, s^{-1})	343 ± 31	9.3 ± 0.5^d
ATP binding (actomyosin), $n = 3^e$		
$K'_{1T}k'_{+2T}$ (μ M $^{-1}$ · s^{-1})	1.7 ± 0.2	0.4 ± 0.1^b
$K'_{0.5}$ (μ M)	577 ± 172	918 ± 224
k'_{+2T} (s^{-1})	1003 ± 157	404 ± 60
Recovery stroke, $n = 3^f$		
k_{+RCF} (fast phase, maximum rate, s^{-1})	479 ± 14	906 ± 50^b
$K_{0.5}$ (μ M)	191 ± 16	470 ± 53^b
k_{+RCS} (slow phase, maximum rate, s^{-1})	32 ± 3	17 ± 1^b
Pyrene actin binding: M.ADP.P _i (μ M $^{-1}$ · s^{-1}), $n = 1^e$		
k_{+Pi} (maximum rate, s^{-1})	6.7 ± 0.4	0.6 ± 0.1
Actin-activated phosphate release, $n = 1^g$		
$K_{Assoc} \times k_{+Pi}$ (actin concentration dependence, μ M $^{-1}$ · s^{-1})	19.4 ± 4.0^h	0.9 ± 0.1
k_{+Pi} (maximum rate, s^{-1})	206 ± 34^h	N.D.
Power stroke, $n = 3^f$		
$K_{Assoc} \times k_{PWF}$ (actin concentration dependence, μ M $^{-1}$ · s^{-1})	19.4 ± 0.9	0.9 ± 0.1^d
k_{+PWF} (fast phase, maximum rate, s^{-1})	417 ± 95	N.D.
k_{+PWS} (slow phase, maximum rate, s^{-1})	94 ± 36	N.D.
Actomyosin ADP Release, $n = 5$		
k'_{+D} (s^{-1}) ⁱ	25.2 ± 1.8	46.1 ± 6.0^d

^aSteady-state ATPase measurements.

^b $p < 0.01$.

^cIntrinsic tryptophan fluorescence.

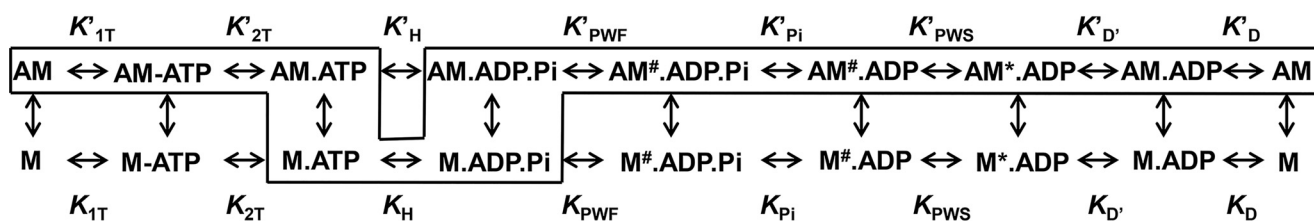
^d $p < 0.0001$.

^ePyrene actin.

^fFRET.

^gMDCC-PBP fluorescence.

^hThe data are from Ref. 22.

ⁱ*mant*ADP fluorescence.


Scheme 1

fold and increased the K_{ATPase} (the actin concentration at which ATPase is half-maximal) 5-fold (Fig. 1B and Table 1), which was similar to the previous myosin V study (26).

Transient and structural kinetic properties

We performed transient and structural kinetic analysis to determine how the S217A mutation impacts the key structural and biochemical transitions in the myosin ATPase cycle. The data were analyzed based on the established kinetic scheme (Scheme 1) of the ATPase cycle also utilized in recent manuscripts (18, 22). In Scheme 1, the rate constants going from left to right are indicated with a positive subscript (e.g. k_{+i}), whereas those going right to left have a negative subscript (e.g. k_{-i}).

The rate of ATP binding and hydrolysis in the absence of actin was measured by mixing MV 1IQ with varying concentrations of ATP and monitoring the enhancement in tryptophan fluorescence (Fig. S1). The data were fit to a hyperbolic func-

tion, and the maximum rate of tryptophan fluorescence change was determined, which is thought to report the ATP hydrolysis rate constant ($k_{+H} + k_{-H}$). The second-order binding constant for ATP binding to myosin can be obtained by determining the slope of linear portion of the curve at low ATP concentrations ($K_{1T}k_{+2T}$). We found that S217A reduces the maximum rate of ATP hydrolysis 40-fold while slightly enhancing the second-order binding constant for ATP binding to myosin (Fig. S1 and Table 1).

ATP binding to myosin triggers movement of the lever arm into the pre-power stroke state (recovery stroke), which is important for priming myosin for force generation. The rate of the recovery stroke was examined by monitoring the FRET signal associated with the FLaSH-QSY donor-acceptor pair upon mixing MV-F:QSY-CaM with varying concentrations of ATP (Fig. 2, A-C). The FLaSH fluorescence increase was best fit to a two-exponential function at most ATP concentrations (Fig. 2C). The amplitude of the fast phase dominated the signal (90%

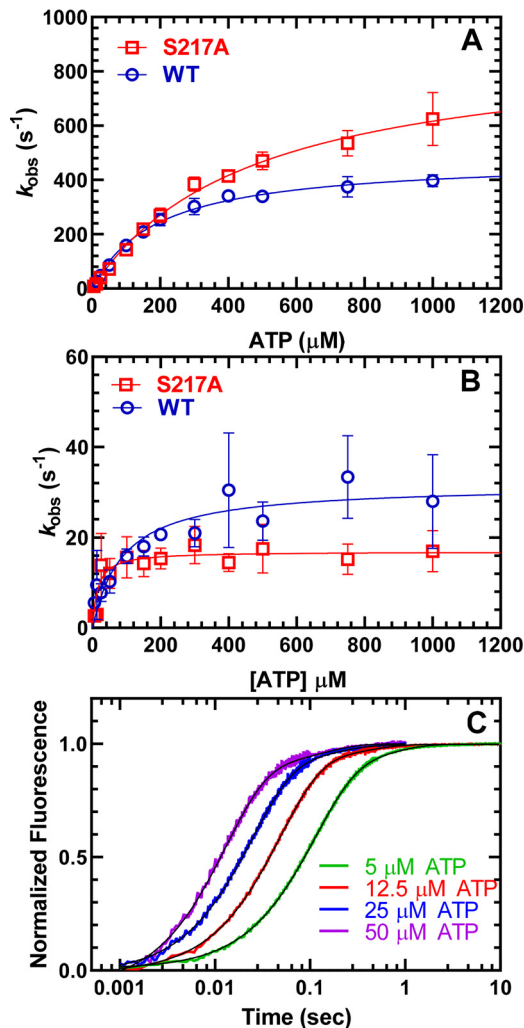


Figure 2. Structural kinetic measurements of the recovery stroke. The recovery stroke was measured by mixing MV-F.QSY-CaM with varying concentrations of ATP and monitoring the enhancement in donor fluorescence. The fluorescence transients were best fit by a two-exponential function at most ATP concentrations, whereas the fast phase was more than 90% of the fluorescent signal. *A* and *B*, the fast phase (*A*) and the slow phase (*B*) of the fluorescence transients were hyperbolically dependent on ATP concentration. *C*, representative fluorescence transients with S217A at four different ATP concentrations. The rate constants (\pm S.E.) of the fast phase were 11.6 ± 0.2 , 24.1 ± 0.2 , 45.5 ± 0.3 , and $81.9 \pm 0.4 \text{ s}^{-1}$ at 5, 12.5, 25, and 50 μM ATP, respectively, whereas the slow phase ranged between 5 and 10 s^{-1} . The data points in *A* and *B* represent means \pm S.D. from three separate experiments with three separate protein preparations.

or greater) in both S217A and WT. By fitting the fast and slow rate constants to a hyperbolic function, we determined that S217A increases the maximum rate of the fast recovery stroke rate constant (k_{+RCF}) (Fig. 2*A*), whereas the slow phase of the recovery stroke (k_{+RCS}) (Fig. 2*B*) was fairly similar to WT. Because the slower phase of the recovery stroke represents a small fraction of the total signal, we have not attempted to include this transition in our kinetic modeling.

Myosin adopts a weak actin-binding conformation upon binding to ATP that dramatically weakens its affinity for actin. Pyrene actin is quenched when myosin is tightly bound to actin, and upon ATP binding there is an increase in pyrene fluorescence that can be used to monitor the rate of ATP binding and maximum rate of transition into the weak binding states (Fig.

S2). In S217A the fluorescence transients were best fit to a two-exponential function, and the fast phase was \sim 70% of the signal, whereas in WT most transients were single-exponential. We found that S217A decreases the maximum rate of ATP-induced transition into the weak binding states (k'_{+2T}) (2-fold) and second-order rate constant ($K'_{1T}k'_{+2T}$) for ATP binding (4-fold) (Fig. S2 and Table 1). The slower phase of the ATP-induced dissociation transients may be associated with an isomerization prior to ATP binding found in other myosins (30).

The power stroke and phosphate release rate constants are accelerated when myosin with the products of ATP hydrolysis in the active site (M.ADP.P_i) binds to actin (Fig. 3). We performed sequential mix experiments to examine the actin-activated power stroke and phosphate release rate constants. We monitored the FRET signal upon mixing MV-F.QSY-CaM with substoichiometric ATP, allowing the reaction to age for 20 s and then mixing with varying concentrations of actin. The FLASh fluorescence transients used to monitor the change in FRET were best fit by a two-exponential function (Fig. 3*C*). In WT, the fast and slow power stroke rate constants were hyperbolically dependent on actin concentration as we previously reported (18, 22) (Fig. 3*A*). The fast and slow phases of the FRET transients were linearly dependent on actin concentration in S217A (Fig. 3*B*). Although the maximum rate of the fast power stroke was not determined for S217A, the actin dependence of the fast power stroke rate constant was found to be 20-fold slower in S217A than WT ($K_{\text{Assoc}} \times k_{\text{PWF}} = 0.9 \pm 0.1$ versus $19.4 \pm 0.9 \mu\text{M}^{-1} \cdot \text{s}^{-1}$, respectively). Similarly, the slow power stroke was 5-fold slower at 30 μM actin in S217A compared with WT.

We examined the phosphate release rate constant using unlabeled MV constructs and a sequential mix setup identical to that described above, except that the phosphate-binding protein was present, which allowed phosphate release to be measured as a function of actin concentration. The phosphate release transients were best fit by a single-exponential burst (P_i release) followed by a second slow phase (prehydrolysis intermediates) (Fig. 3*D*). In WT, the phosphate release rate constant was hyperbolically dependent on actin concentration and significantly slower than the fast power stroke rate constant (22) (Fig. 3*A* and Table 1). However, the rate constant of the phosphate burst was linearly dependent on actin concentration in S217A ($K_{\text{Assoc}} \times k_{+P_i} = 0.9 \pm 0.1 \mu\text{M}^{-1} \cdot \text{s}^{-1}$) and nearly identical to the fast power stroke rate constant (Fig. 3*B*).

The dramatic decrease in the actin dependence of the power stroke and phosphate release of S217A prompted us to directly measure the rate of binding to actin in the M.ADP.P_i state (Fig. 4). We performed a sequential mix experiment in which myosin was first mixed with ATP (10 μM), aged for 20 s to allow ATP binding and hydrolysis, and then mixed with varying concentrations of pyrene actin (5–10-fold excess over myosin) and saturating ADP (0.5 mM ADP, included to prevent multiple turnovers). The fluorescence transients were fit to a single-exponential function at all pyrene actin concentrations. The rate of pyrene actin quenching was linearly dependent on actin concentration, and the slope of the linear dependence was 10-fold

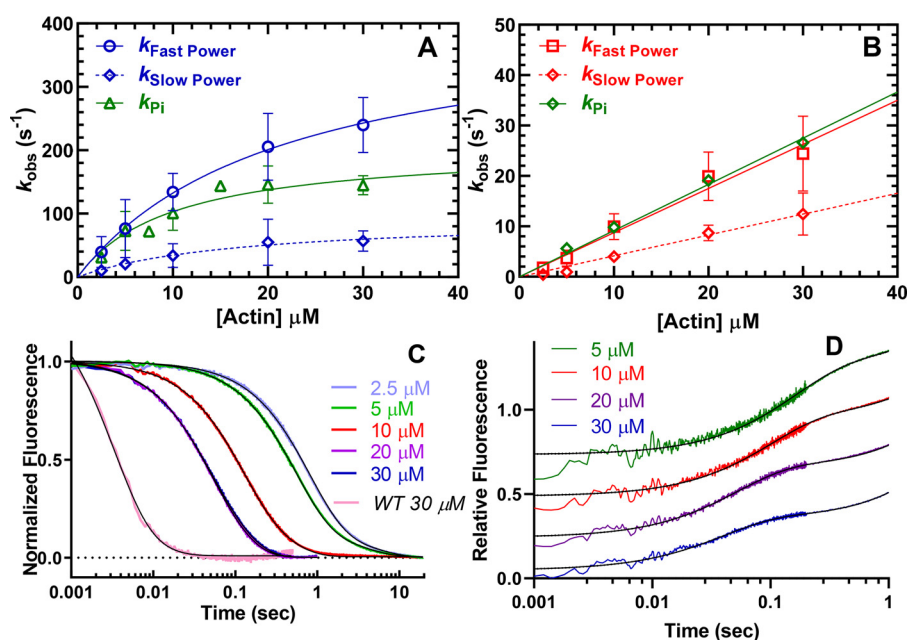


Figure 3. Structural kinetic measurements of the power stroke compared with phosphate release. The power stroke was monitored by examining donor fluorescence quenching after mixing MV-F.QSY-CaM first with ATP, aging the reaction for 20 s to allow hydrolysis, and then mixing with varying concentrations of actin. **A**, in WT, the fluorescence transients were best fit by a two-exponential function, and both the fast ($k_{\text{Fast Power}}$) and slow ($k_{\text{Slow Power}}$) phases of the power stroke were hyperbolically dependent on actin concentration (previous experiments reported in Refs 18 and 22 were included as part of the data set). The phosphate release rate constant was also monitored with nearly identical conditions as above except the presence of MDCC-PBP allowed detection of the change in P_i concentration (data are from Ref. 22). **B**, in S217A, the fluorescence transients were also best fit by a two-exponential function, whereas the rate constants of the fast and slow phases were linearly dependent on actin concentration. The phosphate release rate constants were nearly identical to the fast power stroke rate constants in S217A. **C**, representative fluorescence transients from the power-stroke experiments in S217A (2.5–30 μM) ($k_{\text{Fast Power}} = 26.1 \pm 0.4 \text{ s}^{-1}$, $k_{\text{Slow Power}} = 9.5 \pm 0.1 \text{ s}^{-1}$ at 30 μM actin, \pm S.E.) and WT (30 μM) ($k_{\text{Fast Power}} = 302.0 \pm 5.1 \text{ s}^{-1}$, $k_{\text{Slow Power}} = 54.9 \pm 3.4 \text{ s}^{-1}$ at 30 μM actin, \pm S.E.). **D**, representative fluorescence transients of the phosphate release transients in S217A fit to a two-exponential function ($k_{\text{P}_i} = 5.6 \pm 0.1, 9.8 \pm 0.1, 19.1 \pm 0.1, 26.6 \pm 0.1 \text{ s}^{-1}$, \pm S.E. with a slow phase between $0.5\text{--}2 \text{ s}^{-1}$ at 5, 10, 20, 30 μM actin). The data points in **A** and **B** represent means \pm S.D. from at least three separate experiments with three separate protein preparations.

decreased in S217A ($0.6 \pm 0.1 \mu\text{M}^{-1}\cdot\text{s}^{-1}$) compared with WT ($6.7 \pm 0.4 \mu\text{M}^{-1}\cdot\text{s}^{-1}$).

After the power stroke and phosphate release occur, myosin with ADP bound remains tightly bound to actin until ADP is released and ATP-induced dissociation occurs. We examined the ADP release rate constant in acto-MV using *mant*ADP. A complex of acto-MV (0.5 μM) and *mant*ADP (10 μM) was mixed with excess ATP (1 mM). The *mant*ADP fluorescence decrease was used to determine the ADP release rate constant and was fit to a single-exponential function. We found that the *mant*ADP release rate constant (k'_{+D}) was 2-fold faster in S217A compared with WT (Table 1).

We performed kinetic simulations using Kintek Explorer software, which allowed us to fit fluorescence transients from the power stroke and phosphate release experiments to the kinetic model in Scheme 1 (Fig. S3). The rate constants used in the simulations are shown in Table S1. We also generated synthetic data of the power stroke and phosphate release transients using the kinetic model and fit the synthetic data to an appropriate exponential function, which allowed us to create a simulated data set of the power stroke and phosphate release in WT and S217A (Fig. S4). The synthetically generated data were similar to the experimental data. We also generated actin-activated ATPase curves using the kinetic model that were similar to our experimental data (Fig. S5). Interestingly, the experimental data fit well to a kinetic model in which S217A does not alter the maximum rate of the fast power stroke (k'_{PWF}) or phos-

phate release (k'_{P_i}), demonstrating that the mutation slows actin dependence of these steps by altering the actin association step (K_{Assoc}). Overall, our kinetic models support the conclusion that the S217A mutant alters several steps in the ATPase cycle including ATP-induced dissociation (2-fold), hydrolysis (40-fold), and ADP release (2-fold), which was also demonstrated in the Forgacs *et al.* study (26). One difference between the two studies is that the maximum rate of phosphate release was slowed \sim 10-fold in the work of Forgacs *et al.* (26) (16 s^{-1} versus 198 s^{-1} , respectively) without changing the actin dependence of P_i release, whereas in our study we found the S217A mutation weakened the actin dependence of P_i release (20-fold). The Forgacs *et al.* (26) study was done at lower ionic strength and temperature, and the affinity of myosin for actin in the M.ADP. P_i state is known to be ionic strength dependent (see “Discussion”). Thus, our current results with S217A are quite consistent with previous studies and suggest that the main impact of the mutation is on the hydrolysis and actin-activated P_i release steps.

Transient time-resolved FRET

To quantitate the effect of the S217A mutation on the distribution of structural states within MV, we utilized transient time-resolved FRET (TR²FRET, Fig. 5). A 5000-Hz pulsed laser and subnanosecond detection of the resulting fluorescence transients from MV-F.QSY-CaM samples for both WT and S217A in various biochemical states were acquired following

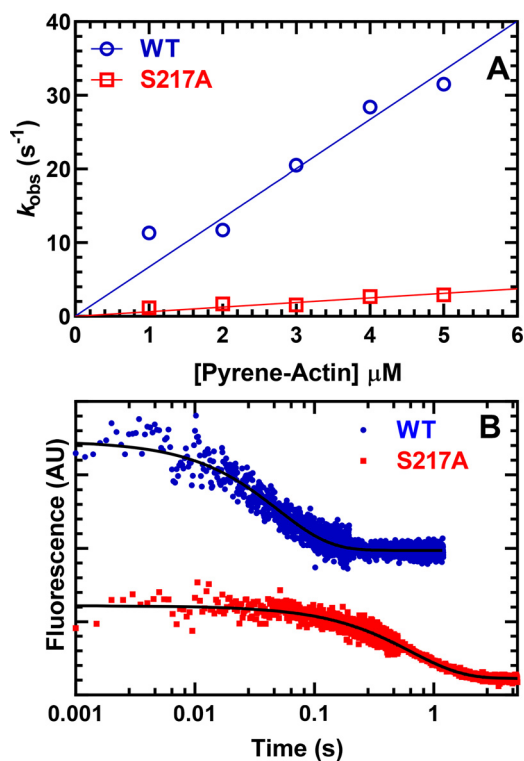


Figure 4. Pyrene actin binding in the M.ADP.P_i state. The rate of pyrene actin quenching was monitored with a sequential mix experiment similar to that described in Fig. 3, such that myosin with the hydrolyzed products in the active site (M.ADP.P_i) was mixed with varying concentrations of pyrene actin. *A*, the rate of pyrene actin quenching was linearly dependent on the pyrene actin concentration and ~10-fold slower in the S217A mutant compared with WT. *B*, representative fluorescence transients of pyrene actin quenching (3 μM pyrene actin and 0.5 μM M.ADP.P_i) fit to a single-exponential function ($k_{\text{obs}}=20.5 \pm 0.3$ or 1.6 ± 0.1 s⁻¹ in WT and S217A, respectively).

rapid stopped-flow mixing (Fig. S6). The multiexponential fluorescence waveforms that were acquired were globally fit to a two-Gaussian distance distribution, as reported in our previous publications (18, 22). The two distances of this structural model closely match those predicted from available crystallographic studies, consistent with our previous studies (Table 2) (18, 22). For both the WT and S217A samples in various biochemical states, the mole fractions of molecules in either the pre-power stroke or post-power stroke structural states were allowed to vary. The fluorescence intensity and lifetime changes from the recovery stroke experiments (Fig. 5A and Fig. S7A) are best fit to a mole fraction change from one distance to the other following the stopped-flow mix, from MV in the absence of nucleotide or actin (M(apo)) to MV with hydrolyzed ATP bound (M.ADP.P_i). Similarly, the fluorescence intensity and lifetime changes from the power-stroke experiments (Fig. 5A and Fig. S7B) are best fit as a mole fraction change between the two fit distance distributions from MV with hydrolyzed ATP bound (M.ADP.P_i) to MV bound to actin with excess ADP present (A.M.D). The mole fraction information and the two-Gaussian distance distribution is plotted for both WT and S217A (Fig. 5 and Table 3). The S217A mutation does not affect either the interprobe distances in either structural state or the mole fraction of MV molecules occupying these states for any of the bio-

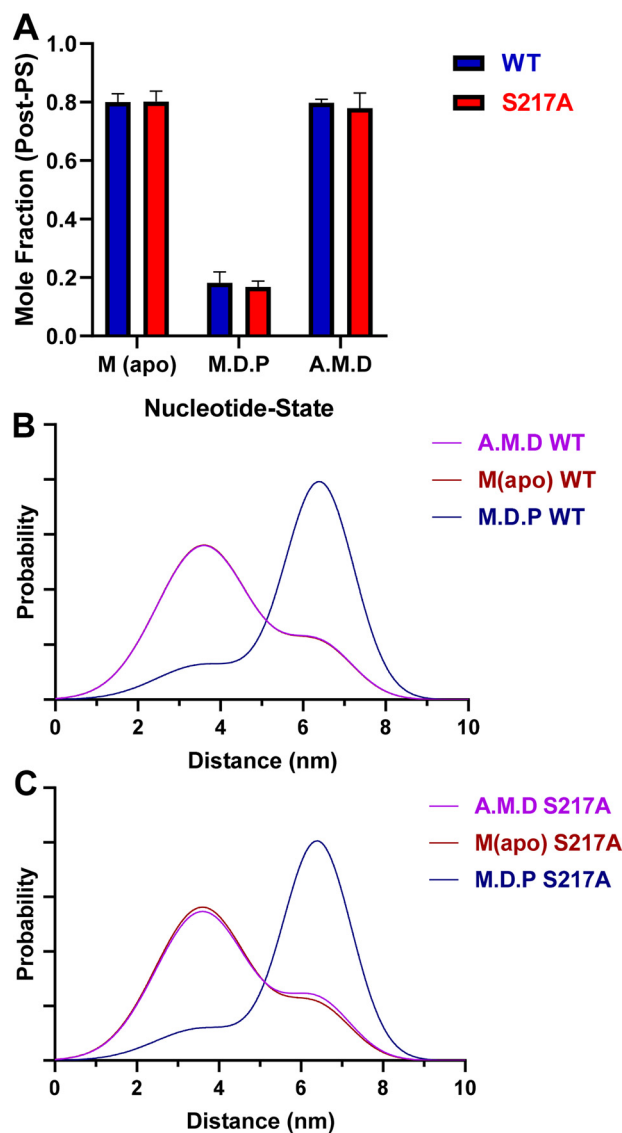


Figure 5. Transient time-resolved FRET measurements. Time-resolved intermolecular FRET within MV-F:QSY-CaM was acquired with 125-ps resolution following excitation with a 5000-Hz pulsed laser. The fluorescence transients for three biochemical states were best fit globally to a two-Gaussian distance distribution corresponding to the two lever arm orientations of the myosin motor protein in its pre- and post-power stroke states (19). *A*, the mole fraction of the post-power stroke structural state for each biochemical state was fit separately for WT (blue) and S217A (red). For the recovery stroke experiment, the corresponding mole fraction change between lever arm orientations is the change from M(apo) to M.D.P. The mole fraction change between the two lever arm orientations for the power-stroke experiment is the change from M.D.P to A.M.D. *B* and *C*, the mole fraction information from *A* and the two-Gaussian distance distribution is plotted for both WT (*B*) and S217A (*C*) (see also Table 2). The peak-center and full-width half-maximum for each distance distribution are shown (see also Table 3).

chemical states acquired. The kinetics of lever arm rotation determined by TR²FRET demonstrate that S217A enhances the recovery stroke rate constant (Fig. S7A) and slows actin activation of the power stroke (Fig. S7B), similar to the results we observed by stopped-flow FRET (Figs. 2 and 3). The observed TR²FRET power stroke rate constants were best fit by a single-exponential function, likely because the experiment was not performed with a sequential mix setup as was done in the stopped-flow FRET experiments.

Table 2**Transient time-resolved FRET parameters**

The transient time-resolved FRET parameters were determined by simultaneously fitting a two-Gaussian distance distribution model to power stroke and recovery stroke data. The error estimates are $\pm 67\%$ confidence interval determined by error plane analysis. All parameters were fit globally.

Construct	Post-power stroke Gaussian		Pre-power stroke Gaussian	
	D ₁	FWHM ₁	D ₂	FWHM ₂
WT	35.9 \pm 1.4	26.8 \pm 4.5	64.0 \pm 0.4	19.6 \pm 2.5
S217A				

Table 3**Mole fractions of MV lever arm orientation in the post-power stroke state**

The mole fractions of MV lever arm orientation in the post-power stroke state were determined by simultaneous fitting a two-Gaussian distance distribution model to power stroke and recovery stroke data. The error estimates are $\pm 67\%$ confidence interval determined by error plane analysis. For statistical significance, each of the three nucleotide states of S217A was compared with the corresponding nucleotide state in WT; no significant differences were found.

Nucleotide state	Construct	
	WT	S217A
M	0.81 \pm 0.01	0.81 \pm 0.01
A.M.D	0.78 \pm 0.01	0.74 \pm 0.05
M.D.P _i	0.20 \pm 0.02	0.18 \pm 0.03

Optical trapping

Both the WT and S217A constructs were adhered to a nitrocellulose-coated coverslip via an anti-Myc antibody in buffer conditions similar to our studies of myosin II (60 mM KCl, 1 mM EGTA, 4 mM MgCl₂, 1 mM DTT, and 100 μ M ATP at pH 7.0). A single actin filament attached to silica beads held in two optical traps was brought into contact with a single myosin molecule in the presence of 100 μ M ATP. Upon strongly binding to the actin filament, myosin causes a reduction in the Brownian motion and a displacement driven by the rotation of the lever arm, *i.e.* working stroke (Fig. 6). Because of Brownian forces experienced by the bead-actin-bead assembly when unbound, unitary displacements can be positive or negative, but the center of the distribution reflects the average unitary displacement (31). Based on several hundred single-molecule binding events for WT ($n = 352$) and S217A ($n = 428$), we found that the average unitary displacement was slightly different for the WT and S217A (3 ± 0.4 and 5 ± 0.4 nm, respectively) (Fig. S8). However, the average lifetime of the binding events was less than half as long for the S217A *versus* WT (107 ± 17 *versus* 251 ± 39 ms) (Fig. S8), which is relatively consistent with the faster ADP release results in solution (Table 1). We also examined the rate constant of the working stroke in the optical trap (*e.g.* overall transition from the weakly/unbound, pre-power stroke state, to the strongly bound, post-power stroke state) by ensemble averaging the positive displacement events (Fig. 6). The rate constant was only slightly different for WT (629 ± 30 s⁻¹) and S217A (867 ± 50 s⁻¹), suggesting that in both constructs the working stroke is very rapid, occurring at a rate of at least 600–800 s⁻¹. The y intercepts of the ensemble averaging demonstrated very similar positive displacement values for WT *versus* S217A (6.9 ± 0.1 *versus* 6.6 ± 0.1 nm). We also did not observe a difference in the frequency of binding events for the

WT *versus* S217A (0.42 ± 0.10 *versus* 0.60 ± 0.15 events/s, means \pm S.E.) (Fig. S9). See Table S3 for summary of optical trapping results.

Discussion

In the current study we used a point mutation (S217A) in a conserved region of the active site of myosins to examine how myosin coordinates structural changes in the active site with structural changes in the lever arm region. We found that the S217A mutation can uncouple the lever arm rotation during the recovery stroke with the chemical step of ATP hydrolysis, clearly demonstrating that these are two separate events in the ATPase cycle. In addition, we found that the S217A mutation slows actin activation of lever arm rotation and P_i release but does not dramatically slow the rate of the working stroke in the optical trapping assay. This suggests that the mutation slows an actin-dependent step that occurs prior to the power stroke and P_i release. We propose that the actin-dependent step is a transition after the initial electrostatic weak binding between actin and myosin but before the transition to the tightly bound closed actin-binding cleft state that is coupled to lever arm rotation and force production.

Impact of S217A on overall enzymatic, structural, and mechanical properties

Our transient kinetic characterization demonstrates that the S217A mutation slows the ATP hydrolysis and actin-activated phosphate release rate constants but accelerates the actomyosin ADP release rate constant. The results are consistent with a previous study of the mutation in mouse myosin VA (26). Therefore, the predominant steady-state intermediates are changed from the actomyosin·ADP state in WT MV to the M. ATP and M.ADP.P_i states in S217A, suggesting that the rates of ATP hydrolysis ($k_{+H} + k_{-H}$) and attachment to actin (k_{+Assoc}) are rate-limiting in the mutant. We also calculated the duty ratio based on the equation outlined in Forgacs *et al.* (26) and found that the mutant reduces the duty ratio ~ 6 -fold (0.15 and 0.89, respectively). Our single-molecule optical trapping results suggest that the S217A mutation does not alter the positive unitary displacements but decreases the attached lifetime (Table S3). The attached lifetime is longer than expected for both WT and S217A based on the ADP release rate constants measured in solution (Table S3), which could be due to the lower temperature of the optical trapping experiments, the mant fluorophore altering the ADP release rate constants in solution, and/or the impact of mechanical load in the optical trap. However, the trend of a 2-fold shorter attached time in S217A is consistent with the 2-fold faster ADP release rate constant measured in solution. Ensemble averaging of the single-molecule records suggests that the displacement generated by the working stroke occurred at a rate of at least 600–800 s⁻¹ and was only slightly different in WT and S217A MV (Fig. 6). The working stroke rate constants are likely an underestimate because the measured rate is limited by the viscous forces acting to slow the velocity of the 1- μ m microsphere moving through solution (32). Thus, it is likely that the working stroke occurs at >1000 s⁻¹ and therefore would be consistent with the rates of 700–5000 s⁻¹ observed under resistive loads in skeletal (33) and cardiac

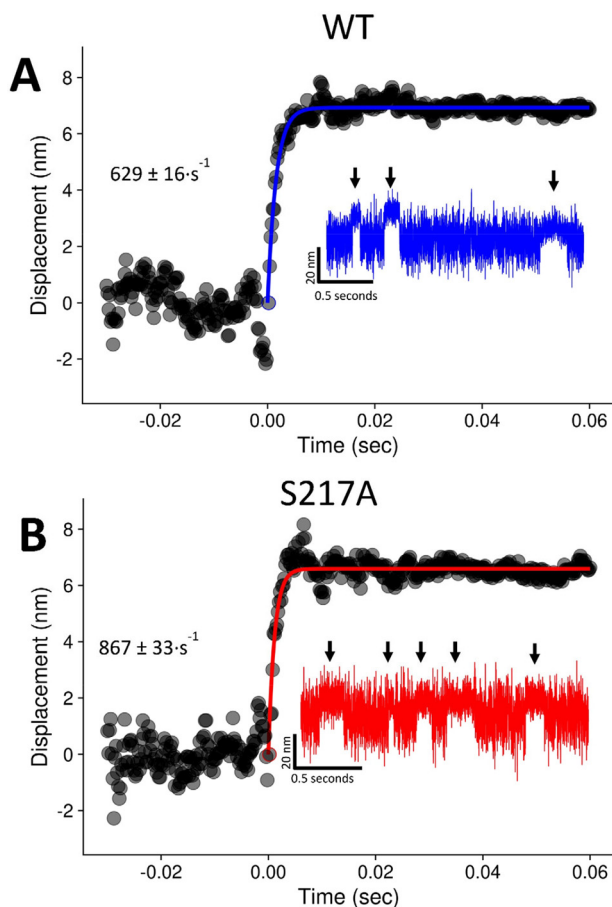


Figure 6. Ensemble average of single-molecule binding events. Single-molecule optical trapping experiments were performed to determine the impact of S217A on the step size and attached time. In addition, the rate of the working stroke was examined by performing ensemble averaging of single-molecule binding events. *A* and *B*, each data point represents the average of 244 and 333 observations for the WT (*A*) and S217A (*B*), respectively. The start of the events were aligned to time 0 and the displacement immediately prior to the binding event. Data were fit, from time 0, with a single exponential to determine the rate of the transition from unbound to bound (means \pm S.E.; see “Experimental procedures” for details about the analysis). The rate of the working stroke was slightly faster in the mutant versus WT ($p < 0.01$), but the positive displacements were similar (see Table S3 for summary). Insets show representative raw displacement records from the single-molecule laser trap assay. Arrows highlight actomyosin strong-binding events.

muscle myosin (21) using an optical trap with microsecond time resolution. Our results suggests that although the mutation may have altered actin activation of the power stroke and P_i release, it did not dramatically reduce the working stroke rate constant and had no impact on the size of the unitary displacements. These findings are also qualitatively consistent with our time-resolved FRET studies, which demonstrated that S217A and WT MV have similar donor–acceptor distance and distance distributions in the pre– and post–power stroke states (Fig. 5). In addition, the mole fractions observed in the pre– and post–power stroke states in different nucleotide states were similar. Overall, the results are consistent with a model in which the S217A mutant does not disrupt the overall conformation of the pre– or post–power stroke conformations, as well as the equilibrium between these states, but alters the kinetics (transition states) of the transitions between these structural states.

Coupling of the recovery stroke and ATP hydrolysis

The recovery stroke in myosin is a key step that allows the energy from ATP hydrolysis to be stored in the myosin motor in a pre–force-generating state. There is strong evidence from structural and solution biochemical studies for how myosin transitions from a nucleotide-free (Apo state) to the ATP-bound transition state in which the active site is primed for ATP hydrolysis and the lever arm is in a pre–power stroke conformation (18, 22, 34–36). ATP binding to Apo myosin causes the conserved elements of the active site, switch I, switch II, and P-loop to form closed conformations in which they coordinate binding to the γ -phosphate. The movement of switch II into the closed conformation is associated with a shift in the relay helix from a straight to a bent conformation, which alters its interactions with the converter domain and helps position the lever arm in the pre–power stroke position (34). Other studies suggested that there is a second phase of the recovery stroke that occurs with hydrolysis, but it was not known whether this second phase is associated with a further change in the lever arm position or simply local rearrangements in the active site and/or converter/relay helix (37). Our results demonstrate that S217A allows for even faster movement of the lever arm into the pre–power stroke conformation, whereas the active site is slower to hydrolyze ATP. The work of Forgacs *et al.* (26) demonstrated that the tryptophan fluorescence signal was nearly identical to the quench flow results, suggesting that the tryptophan fluorescence signal reports hydrolysis in S217A (26). Our work is consistent with a model in which ATP binding rapidly transitions myosin into a pre–power stroke conformation, primarily involving switch II, which is followed by a rearrangement of the active site to hydrolyze the γ -phosphate, involving both switch I and II (Fig. 7). Interestingly, it is the second transition associated with priming the active site for hydrolysis that is sensed by the nucleotide-sensitive tryptophan (Fig. S1). Thus, S217A causes these events to become uncoupled and demonstrates that the transition to the pre–power stroke state is not driven by the energy from hydrolysis but rather ATP binding to switch II, which has been proposed in previous structural (34) and kinetic studies (37). Interestingly, the ATP hydrolysis step may stabilize the pre–power stroke conformation by promoting local conformational changes around the relay helix and converter domain where the nucleotide-sensitive tryptophan is located. Based on Forgacs *et al.* (26), the S217A mutant slows the hydrolysis step without altering the equilibrium constant, and our mole fraction results in the time-resolved FRET studies (Fig. 5) are in agreement with these conclusions. Overall, our studies of the recovery stroke highlight that ATP binding drives the recovery stroke, whereas ATP hydrolysis may stabilize the pre–power stroke conformation and control the number of myosins in an ensemble that are primed to generate force.

Impact of S217A on actin activation of the power stroke

Our results provide evidence that structural changes in the actin-binding region are coupled to changes in the active site during the initial events of the force-generating mechanism. We found that S217A slows actin activation of the power stroke and P_i release in solution, making them essentially appear to

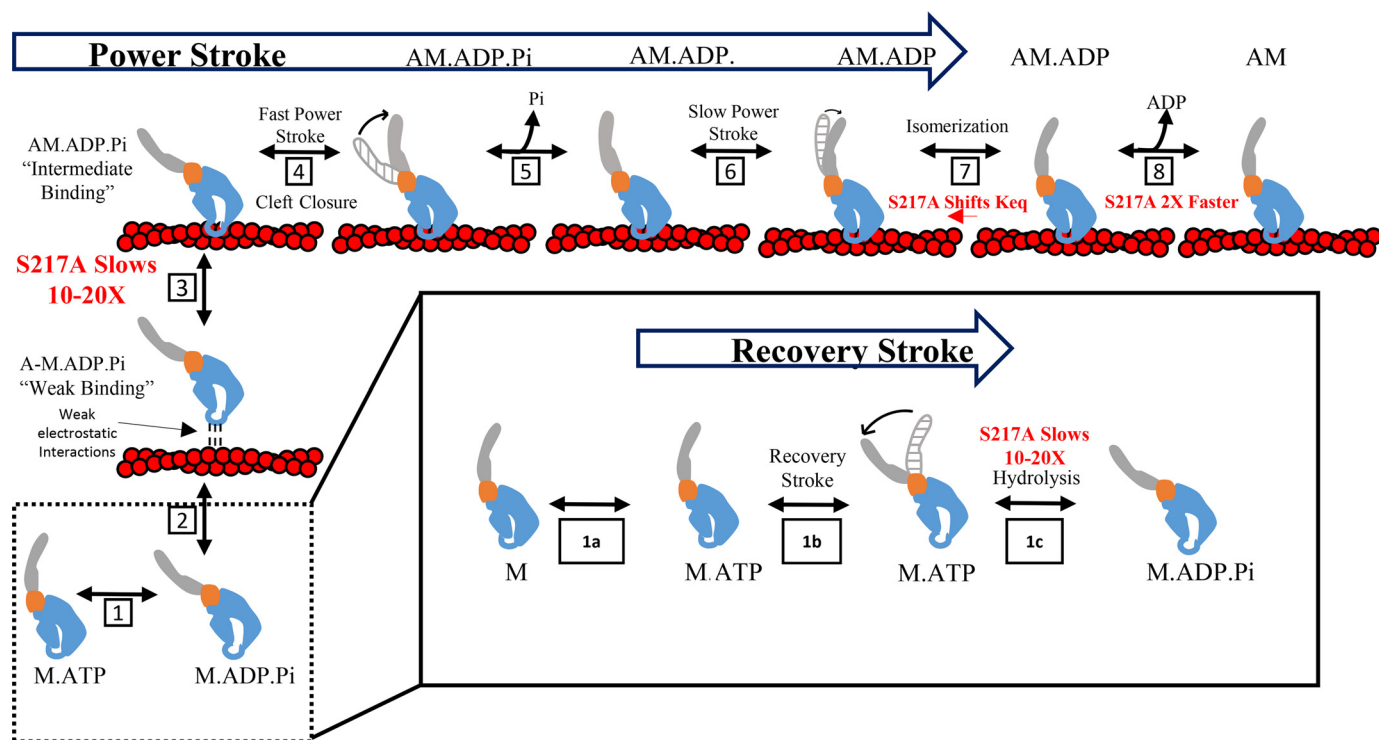


Figure 7. Model of actomyosin ATPase cycle and impact of S217A on specific steps. Myosin binds and hydrolyzes ATP, which produces a recovery stroke that primes its lever arm for force generation (step 1). The inset highlights the key steps of the recovery stroke including formation of a collision complex with ATP (step 1a, K_{1T}), the movement of the lever arm during the recovery stroke (step 1b, K_{2T}), and the hydrolysis of ATP in the active site (step 1c, K_{4T}). Myosin with the products of ATP hydrolysis first binds weakly to actin through electrostatic interactions (step 2, K_{Assoc}) and transitions into the initial force-bearing state with intermediate actin affinity (step 3, K_{Assoc}). In the initial force-bearing state, the actomyosin interface, active site, and lever arm are primed for the power stroke. The fast power stroke is associated with a large rotation of the lever arm, which is coupled to strong actin binding and cleft closure (step 4, K_{PWF}). The release of phosphate into solution occurs after the fast power stroke (step 5, K_{Pi}). This is followed by the slow power stroke (step 6, K_{PWS}), an active site isomerization that reduces the affinity of myosin for ADP (step 7, K'_D), and the release of ADP from the active site (step 8, K'_D).

occur with the same rate constant (Fig. 3), whereas the rate of the working stroke in the single-molecule assay is not dramatically slowed (Fig. 6). This suggests that an actin-dependent conformational change is slowed by S217A making this step rate-limiting in terms of triggering the power stroke and then P_i release. Indeed our pyrene actin-binding studies directly demonstrate that S217A slows the rate of pyrene actin quenching 10-fold. One obvious possibility is that S217A alters the initial weak interaction between actin and myosin; however, this seems unlikely because the mutation is in the active site, and weak binding is thought to be mediated by electrostatic interactions between actin and myosin (38, 39). Alternatively, S217A may impact the transition from the weak binding state to the initial stereospecifically bound force-bearing state with the cleft open immediately prior to the power stroke. Woody *et al.* (21) proposed the initial force-bearing pre-power stroke state based on their ultra-fast optical trapping studies, which found evidence for an actin-attached state that was populated prior to the working stroke, strong actin binding, and P_i release (21, 33). We also propose that the initial force-bearing state is not a structural state capable of releasing phosphate (e.g. the PiR proposed by Llinas *et al.* (17)), because we demonstrate that P_i release only occurs after the power stroke, which is likely coupled to cleft closure (strong actin binding), based on the mechanical step and strong-binding occurring concomitantly in the laser trap assay (Fig. 6). In addition, S217A would not be expected to alter the PiR state, because PiR is mostly associated with changes in switch II with no major

changes in switch I (17), although the S217A mutation could allosterically alter the conformation of switch II. However, it is possible that structural changes in switch I were not observed in the PiR crystal structure because actin binding is required to alter the conformation of switch I. Indeed, there is strong evidence that switch I is crucial for coupling the actin- and nucleotide-binding regions (40).

Another possible scenario is that S217A slows the power stroke directly, which would have to occur before P_i release and thus would become rate-limiting. We do not favor this hypothesis because slowing the power stroke step without altering actin binding does not agree with the 20-fold decrease in the actin dependence of the power stroke (Fig. 3), the pyrene actin quenching data (Fig. 4), and our simulations (Figs. S3 and S4). Also, the rate of the working stroke, which is rapid and similar in WT and S217A in the single-molecule laser trap assay, is not consistent with a slower power stroke in S217A (Fig. 6). Thus, we propose that the S217A mutation impacts the ability to form the initial force-bearing state, suggesting that the active site must undergo actin-dependent structural changes, presumably involving switch I, before this important initial force-bearing state can form.

Updated model of force generation in myosin V

The impact of S217A on actin activation of the power stroke and P_i release provides key insight into models that describe

the sequence of events associated with force generation in myosins (Fig. 7). Myosin containing the hydrolyzed products in the active site (M.ADP.P_i) forms a weak binding interaction with actin with the lever arm in the pre-force-generating state and the switch elements in the active site in closed conformations. Strengthening of the actin-binding interface to form the initial force-bearing state requires structural changes in the active site. The formation of the initial force-bearing state is followed by lever arm rotation and actin-binding cleft closure, which are tightly coupled, and then P_i release occurs from a closed cleft conformation. Our results do not distinguish whether P_i release occurs through the back door (opening of switch II) (4, 17) or through the trap door (opening of switch I) (41, 42). It is possible that the P_i enters the phosphate tunnel shortly after formation of the initial force-bearing state and that P_i is released after the power stroke and cleft closure, as suggested in recent models (4, 43). However, our data would put constraints on the lifetime of such a state with P_i in the phosphate tunnel (~5 ms), based on P_i entering the tunnel before the power stroke and leaving at the observed 200 s⁻¹ rate constant. An excellent test of this model would be to trap P_i in the tunnel with mutations that do not disrupt entry into the tunnel but prevent its release after the power stroke. Woody *et al.* (21) demonstrated that P_i rebinding in the presence of load can reverse the working stroke, providing strong evidence for the power stroke occurring before phosphate release. Therefore, we favor a model in which the lever arm rotation associated with the power stroke occurs rapidly with P_i still in the active site (or in the tunnel), followed by the release of P_i from an intermediate-power stroke and closed actin-binding cleft conformation.

The slower phase of the power stroke that occurs during the actomyosin·ADP states is also slower in S217A, but because the earlier steps are slowed (actin-activated power stroke), it is difficult to evaluate whether it is altered by the mutation and hence the role of switch I in the process. Our simulations do suggest that the equilibrium constant for this state is reduced (Table S1) which may have implications for its ability to transition between actomyosin·ADP states in the presence of external loads (*e.g.* mechanosensitivity).

The proposed model that phosphate release occurs after the power stroke and cleft closure is in agreement with previous biochemical and biophysical studies. In myosin V, phosphate release occurs at an observed rate of ~200 s⁻¹, whereas the rate of the power stroke is clearly faster based on FRET measurements (~400 s⁻¹) (18, 22). In addition, the optical trapping results in the current work and in previous studies with microsecond time resolution are consistent with a rapid working stroke, which we assume is driven by rapid lever arm rotation, and followed by a slower observed phosphate release (21, 33). Most models assume that closure of the actin-binding cleft occurs concomitantly with the power stroke because strong attachment to actin would be required for force production. In support, our previous FRET results demonstrated that the actin-binding cleft closes rapidly before P_i release and pyrene actin quenching (44). However, we proposed that pyrene quenching does not report the cleft closure but another slower transition that is sensed by the actin filament upon strong binding. This hypothesis is consistent with the slower rate of pyrene

actin quenching (Fig. 4) compared with the actin dependence of the power stroke (Fig. 3 and Table 1). Overall, the current solution biochemistry, structural, and single-molecule studies are consistent with the proposed model, but the exact structural details of the actin-binding interface, active site, and lever arm will need to be fully delineated.

Studies in muscle fibers support a model in which there is a force-bearing state populated prior to force generation, which is followed by the power stroke and then P_i release (45). The strongest evidence is from studies that used caged phosphate to demonstrate that P_i rebinding can reverse the force-generating event in the presence of load, suggesting that P_i release occurs after the power stroke (45, 46). Other models in which P_i rebinding accelerates detachment from a post-power stroke state have also been proposed to explain observations in the motility assay (47, 48). Additionally, other muscle fiber studies suggest there is flexibility in terms of when P_i release occurs in relationship to the power stroke, which would indicate that the power stroke does not gate P_i release (49, 50). However, this model is difficult to reconcile with the rapid working stroke rates observed in the ultra-fast optical trapping assay, because a slower P_i release before the power stroke would greatly slow the working stroke (21). Finally, it is important to note that P_i release is impacted by load, as is indicated by optical trapping results (21), and the model proposed here reflects the unloaded situation.

Conservation and variation in the myosin force-generating mechanism

Myosins have very different rates of ATPase cycling and force generation, which allows them to perform specific biological functions. What steps in the proposed model are likely important for kinetically tuning myosins for their functional role in the cells? Myosin V is a processive myosin that can function as a single molecule to transport cargo along actin by spending a large fraction of its ATPase cycle bound to actin and allowing it to walk in a hand-over-hand manner (51, 52). In contrast, muscle myosins function as an ensemble and only interact with actin for a small fraction of their ATPase cycle (53). Therefore, the overall rate of weak-to-strong transition is crucial for controlling the rate of entry into the force-bearing states. Myosin V has a higher affinity for actin than myosin II in the weak-binding states, suggesting that it has a faster rate of association and thus can more rapidly find its next binding site on actin (54). It is possible that myosin V is tuned to rapidly transition from the weak-binding to the initial force-bearing state, which involves enhanced coupling between the active site and actin-binding regions. Indeed, loop 2 in the actin-binding region was found to be involved in enhancing the affinity of myosin V for actin in the weak-binding states (39, 55), and myosin V has several additional positively charged residues in this loop that are known to enhance overall weak-binding affinity (38). Another important charged loop in the actin-binding interface, called the activation loop, was found to be important for actin activation of ATPase activity (56). Therefore, surface loops in the actin-binding region, which tend to vary greatly between myosin isoforms (57), likely play a crucial role in allosterically coupling

actin binding with structural changes in the active site. In addition, actin-regulatory proteins such as troponin-tropomyosin may also be involved in coupling the actin- and nucleotide-binding regions that are important for mediating activation of the power stroke. Indeed, the rate of attachment to actin and phosphate release were demonstrated to be altered by the presence of troponin/tropomyosin in skeletal muscle (58–60).

Conclusions

The current study utilized FRET and optical trapping to provide clear evidence that actin-dependent conformational changes in the active site are required to trigger the power stroke and force generation in myosin V. Our results are consistent with models in which the mechanical step (power stroke and strong actin binding) occurs first, which is followed by a highly irreversible chemical step (P_i release) to thermodynamically drive the reaction forward (18, 19). Variability in the degree of coupling between the actin- and nucleotide-binding regions could explain important differences in the rate of attachment to actin observed in low and high duty ratio myosins. We have identified the switch I region as an important element of the active site that couples the actin- and nucleotide-binding regions during the initial phases of force generation. Other details about how actin binding changes the active site and specifically communicates that to the converter/lever arm will be the subject of future studies.

Experimental procedures

Reagents

We prepared ATP and ADP fresh from powder using reagents of the highest commercial availability, and concentrations were determined by absorbance at 259 nm ($\epsilon_{259} = 15,400 \text{ M}^{-1} \cdot \text{cm}^{-1}$). The chromophores, QSY-9, pyrene idoacetamide, and fluorescein bis-arsenical hairpin binding dye (FLAsH) were purchased from Molecular Probes/Thermo Fisher. The fluorescently labeled phosphate-binding protein (MDCC-PDP) was prepared as described (61). *mant*ADP was purchased from Jena Biosciences.

Protein construction, expression, and purification

We used the same chicken myosin V construct that was used for our previous studies, containing the first IQ domain (residues 1–792), N-terminal tetracysteine motif, and C-terminal Myc and FLAG tags (5, 18, 22, 29). We introduced the S217A point mutation into this construct using QuikChange site-directed mutagenesis (Stratagene). All constructs were coexpressed with calmodulin (CaM) in the baculovirus system and purified by FLAG affinity chromatography. Labeling with FLAsH and exchange of QSY-CaM was performed as previously described (18, 22). Actin was purified from rabbit skeletal muscle (62) obtained from Pell-Freez and labeled with pyrene when necessary (63). We performed all experiments in KMg50 buffer (10 mM imidazole-HCl, 50 mM KCl, 1 mM EGTA, 1 mM MgCl_2 , and 1 mM DTT) at pH 7.0 and 25 °C. We replaced DTT with TCEP in all experiments involving FLAsH labeling. The expression and purification of both WT and S217A MV 1IQ (MV) constructs coexpressed with calmodulin gave similar yields and puri-

ties compared with our previous work (18, 22, 27–29). The steady-state and transient kinetic measurements comparing the mutant and WT were mostly performed in parallel in KMg50 buffer at 25 °C to allow direct comparison to our previous work. For the structural kinetic experiments, WT and S217A constructs contained QSY-CaM and N-terminal FLAsH (MV-F.QSY-CAM) (with 90–100% labeling efficiency) were also performed in parallel in KMg50 TCEP at 25 °C, unless otherwise noted.

Steady-state ATPase activity

We examined steady-state actin-activated ATPase activity using the NADH coupled assay (18, 22, 29). The maximum rate of ATPase rate (k_{cat}) and actin concentration at half-maximal ATPase (K_{ATPase}) was determined from the hyperbolic fits of the ATPase activity as a function of actin. The basal ATPase activity (v_0) was determined in the absence of actin. The average of at least three separate protein preparations was used to compare conditions. An unpaired Student's *t* test was used to determine significant differences between WT and S217A.

Transient kinetic measurements

Examination of the major steps in the actomyosin ATPase cycle was performed using transient kinetic analysis (18, 22, 64). An Applied Photophysics stopped-flow apparatus with a dead time of 1.2 ms and 9.3-nm band pass was used for all measurements. The intrinsic tryptophan fluorescence was monitored by exciting the sample at 290 nm and measuring the emission with a 320-nm long-pass filter. The *mant*ADP fluorescence was monitored by exciting the *mant* fluorescence at 290 nm and measuring the emission with a 395-nm long-pass filter. The pyrene actin fluorescence was excited at 365 nm, and the emission was measured with a 395-nm long-pass filter. We used 380 nm to excite MDCC-PBP, and the emission was measured with a 425-nm long-pass filter. The FRET signal was monitored by exciting FLAsH at 488 nm and measuring the emission with a 515-nm long-pass filter. KinTek Explorer was used to evaluate kinetic models and determine the key steps altered by the S217A mutation. An unpaired Student's *t* test was used to determine significant differences between WT and S217A. The duty ratio was calculated with the following equation (26):

$$d_{\text{ratio}} = \left[\frac{(k_{+H}k'_{+Pi})}{(k_{+H} + k'_{-Pi})} \right] / \left[\frac{(k_{+H}k'_{+Pi})}{(k_{+H} + k'_{+Pi})} + k'_{-D} \right] \quad (\text{Eq. 1})$$

Transient time-resolved FRET

Analysis of the structural distribution of MV lever arm orientations was performed using TR²FRET. All experiments were performed using a 473-nm, 5000-Hz pulsed laser with 1.0-ns FWHM and a *Biologic USA* SFM/20 single-mix stopped flow apparatus with 1.8-ms dead time and acquired with a fluorescence spectrophotometer with 125-ps resolution after passing through a 520/15-nm *Semrock* bandpass filter. The fluorescence lifetime of the donor-only samples (MV-F) was fit for both WT and S217A ($n = 12$ each, from two independent

preparations) using FargoFit data analysis software to obtain both lifetimes and amplitudes (65). The multiexponential lifetimes of the donor-plus-acceptor samples (MV-F.QSY-CaM) were best fit to a two-Gaussian distance distribution, consistent with a motor protein isomerizing between two structural states during its ATP-driven kinetic cycle, as described in our previous publications along with detailed descriptions of the data analysis (19). For the recovery stroke experiments, 80 nM MV-F.QSY-CaM was mixed with 0–1.0 mM ATP (postmix concentrations). Similarly, for the power-stroke experiments, 80 nM MV-F.QSY-CaM and 5.0 μ M ATP was mixed with 5.0 mM ADP and 0–40 μ M actin. To reduce the signal-to-noise ratio to below 1%, several acquisitions were averaged, depending on the length of acquisition. 500 or more fluorescence waveforms were acquired for all transient experiments. For every ATP and actin concentration for the recovery-stroke and power-stroke experiments, the data and standard deviations reported represent $n \geq 6$ from two independent protein preparations. All experiments were performed at 25.0 °C, regulated with a circulating water bath, and performed in KMG50 buffer with TCEP at pH 7.0.

Optical trapping

The assay to determine the single-molecule mechanics and kinetics was performed as previously described (66), with minor modifications to accommodate the myosin V IIQ constructs. Briefly, the myosin was adhered to a nitrocellulose-coated coverslip with 3- μ m silica microspheres serving as pedestals for the myosin. Myosin was added at a concentration of 0.02 μ g/ml to a flow cell precoated with anti-Myc antibody to provide a substrate for myosin binding. The surface was then blocked with BSA to prevent nonspecific interactions between the actin filament and the antibody or surface. The experimental buffer included streptavidin-coated 1- μ m silica microspheres, biotin/TRITC-labeled actin, oxygen scavengers, and 100 μ M ATP, in addition to 60 mM KCl, 1 mM EGTA, 4 mM MgCl₂, and 1 mM DTT at pH 7.0. By maneuvering the piezo-controlled stage, the actin was attached to the optically trapped 1- μ m microspheres and stretched such that 3–4 pN of pretension was applied to the filament. The two-trap stiffness of the assembly was 0.03 pN/nm. Individual pedestals were interrogated by lowering the bead–actin–bead assembly near the surface. Only 1 in 12 pedestals displayed activity, ensuring we were in a single-molecule regime. The data were collected at 5 kHz and analyzed to identify individual events using hidden Markov modeling, as previously described (67), algorithm in R. Change point analysis (68) was used to locate the start and finish of each event. To determine the rate of the transition from weakly/unbound to strongly bound, the positive displacement events were subjected to an ensemble averaging analysis, with minor modifications to previously described methods (69), and fit to a single exponential to determine the rate constant of the working stroke. Statistical differences between WT and S217A were examined with an unpaired Student's *t* test.

Single-molecule laser trapping analysis

Single-molecule binding events were identified by applying a two-state hidden Markov (HM) model to the running variance and running mean of the raw trapping data using the *depmixS4* R package (70). The running variance and running mean signals were treated as conditionally independent in the HM model to allow for the detection of events that produced zero displacement. Ultimately, the HM model categorized each window in either of two states, which represented myosin being unattached or attached to an actin filament, respectively. Unitary displacements were determined by taking the maximum window value from the running mean of each event.

The running windows were set at a window width (w) of 30 ms and moved 15-ms ($w_{1/2}$) upon each advancement of the running window. The half-overlapping windows decreased the correlation between neighboring windows and provided a data set that met the assumptions for the HM model's transition matrix (67) increasing the model's ability to reliably detect events. Consequently, the sliding windows decreased the time resolution of the trapping signal by a factor of $w_{1/2}$, resulting in an artificial instrumental dead time of 15 ms. Moreover, because events were identified based upon the running windows, initial estimates of the event durations were approximated ($t_{\text{on-app}}$) by taking the product of the number of windows (n_w) that comprised an event and the conversion factor ($w_{1/2}$) between the length of the processed running window data set and the original data set ($t_{\text{on-app}} = n_w \times w_{1/2}$).

To improve event duration measurements, we took the start and end indices of each event identified by the HM model and multiplied these time points by $w_{1/2}$ to obtain the relative indices where the binding events occurred in the raw data trace. Each event was then subset of the original raw trace, transformed with a 10-ms (nonsliding) running variance, and analyzed with a change point detection algorithm (68). Reanalyzing each event at the original data collection frequency permitted for more diverse and accurate event duration ($t_{\text{on-acc}}$) measures, which were calculated by differencing the change point identified start (cp_{start}) and end (cp_{end}) indices of each event ($t_{\text{on-acc}} = cp_{\text{end}} - cp_{\text{start}}$). If the change point analysis failed to find an optimal start or end of an event, then the $t_{\text{on-app}}$ value was used for the event duration measurement.

Ensemble averaging of single-molecule events was performed with a similar procedure as described previously by others (21, 33, 69) with slight modifications to accommodate for differences in data collection techniques. The ensemble averaged events are 60 ms long and only include events that had positive displacements. Events meeting the inclusion criteria had the back 30% of their lengths removed in preparation for event alignment. The change point analysis provided a new relative time index for the start of each event, and as a result the events could universally be reindexed with the same relative time scale. The first data point in each event was indexed as dp_0 , and thus each event was indexed as $\{dp_0, dp_1, \dots, dp_n\}c$, where dp_n represents either the 300th data point (dp_{299}) in the event (corresponding to the first 60 ms of a longer event) or the last data point of a shorter event ($dp_{<299}$). For short events less than 60 ms in which $dp_n < dp_{299}$, the average displacement of

the event was used to extend the event by $dp_{299} - dp_n$ data points to make all events equal lengths. Events were then aligned horizontally at dp_0 , and all matching dp_x values were averaged together to create the final ensemble. The average ensembles were then fit with a negative mono-exponential equation using the *drc* and *aomisc* R packages to provide estimates of the rate of the working stroke and plot with the *ggplot2* and *cowplot* R packages. Additional programming tools used for building the analysis programs include the *gtools*, *pracma*, and *tidyverse* packages.

Data availability

All data discussed are presented in the article. Any analysis tools from the article will be shared upon request to the corresponding author: Christopher M. Yengo, cm11@psu.edu.

Acknowledgments—We recognize the outstanding technical efforts of Rohini Desetty.

Author contributions—L. K. G., J. A. R., C. P. M., B. D. S., E. P. D., and C. M. Y. data curation; L. K. G., J. A. R., C. P. M., B. D. S., E. P. D., and C. M. Y. formal analysis; L. K. G., J. A. R., WT, JAC, C. P. M., B. D. S., D. D. T., E. P. D., and C. M. Y. writing-review and editing; D. D. T., E. P. D., and C. M. Y. conceptualization; D. D. T., E. P. D., and C. M. Y. supervision; E. P. D. and C. M. Y. writing-original draft.

Funding and additional information—This work was supported by an National Institutes of Health Grants HL127699 (to C. M. Y.) and R01AR32961 and R01AG26160 (to D.D.T.). L. K. G. is supported by National Research Service Award Postdoctoral Fellowship F32DC016788, and W. T. is supported by American Heart Association Predoctoral Fellowship 19PRE34380569. This work was also supported by American Heart Association Grants 14GRNT20450002 and 18IPA34170048 (to E. P. D.). The content is solely the responsibility of the authors and does not necessarily represent the official views of the National Institutes of Health.

Conflict of interest—The authors declare that they have no conflicts of interest with the contents of this article.

Abbreviations—The abbreviations used are: TCEP, tris(2-carboxyethyl)phosphine; TR², transient time-resolved; CaM, calmodulin; mantADP, 2'-deoxy-ADP labeled with *N*-methylanthraniloyl at the 3'-ribose position; TRITC, tetramethylrhodamine isothiocyanate; HM, hidden Markov.

References

- Hartman, M. A., and Spudich, J. A. (2012) The myosin superfamily at a glance. *J. Cell Sci.* **125**, 1627–1632 [CrossRef Medline](#)
- Heissler, S. M., and Sellers, J. R. (2016) Various themes of myosin regulation. *J. Mol. Biol.* **428**, 1927–1946 [CrossRef Medline](#)
- Berg, J. S., Powell, B. C., and Cheney, R. E. (2001) A millennial myosin census. *Mol. Biol. Cell* **12**, 780–794 [CrossRef Medline](#)
- Robert-Paganin, J., Pylypenko, O., Kikuti, C., Sweeney, H. L., and Houdusse, A. (2020) Force generation by myosin motors: a structural perspective. *Chem. Rev.* **120**, 5–35 [CrossRef Medline](#)

- Trivedi, D. V., Nag, S., Spudich, A., Ruppel, K. M., and Spudich, J. A. (2020) The myosin family of mechanoenzymes: from mechanisms to therapeutic approaches. *Annu. Rev. Biochem.* **89**, 667–693 [CrossRef Medline](#)
- Huxley, A. F. (2000) Mechanics and models of the myosin motor. *Philos. Trans. R. Soc. Lond. B Biol. Sci.* **355**, 433–440 [CrossRef Medline](#)
- Holmes, K. C. (1997) The swinging lever-arm hypothesis of muscle contraction. *Curr. Biol.* **7**, R112–R118 [CrossRef Medline](#)
- Tyska, M. J., and Warshaw, D. M. (2002) The myosin power stroke. *Cell Motil. Cytoskeleton* **51**, 1–15 [CrossRef Medline](#)
- Lynn, R. W., and Taylor, E. W. (1971) Mechanism of adenosine triphosphate hydrolysis by actomyosin. *Biochemistry* **10**, 4617–4624 [CrossRef Medline](#)
- Geeves, M. A. (2016) The ATPase mechanism of myosin and actomyosin. *Biopolymers* **105**, 483–491 [CrossRef Medline](#)
- Batters, C., and Veigel, C. (2016) Mechanics and activation of unconventional myosins. *Traffic* **17**, 860–871 [CrossRef Medline](#)
- Sun, Y., and Goldman, Y. E. (2011) Lever-arm mechanics of processive myosins. *Biophys. J.* **101**, 1–11 [CrossRef Medline](#)
- Ishii, Y., Ishijima, A., and Yanagida, T. (2001) Single molecule nanomanipulation of biomolecules. *Trends Biotechnol.* **19**, 211–216 [CrossRef Medline](#)
- Lombardi, V., Piazzesi, G., Reconditi, M., Linari, M., Lucii, L., Stewart, A., Sun, Y. B., Boesecke, P., Narayanan, T., Irving, T., and Irving, M. (2004) X-ray diffraction studies of the contractile mechanism in single muscle fibres. *Philos. Trans. R. Soc. Lond. B Biol. Sci.* **359**, 1883–1893 [CrossRef Medline](#)
- Stehle, R., and Tesi, C. (2017) Kinetic coupling of phosphate release, force generation and rate-limiting steps in the cross-bridge cycle. *J. Muscle Res. Cell Motil.* **38**, 275–289 [CrossRef Medline](#)
- Sweeney, H. L., and Houdusse, A. (2010) Structural and functional insights into the myosin motor mechanism. *Annu. Rev. Biophys.* **39**, 539–557 [CrossRef Medline](#)
- Llinas, P., Isabet, T., Song, L., Ropars, V., Zong, B., Benisty, H., Sirigu, S., Morris, C., Kikuti, C., Safer, D., Sweeney, H. L., and Houdusse, A. (2015) How actin initiates the motor activity of myosin. *Dev. Cell* **33**, 401–412 [CrossRef Medline](#)
- Trivedi, D. V., Muretta, J. M., Swenson, A. M., Davis, J. P., Thomas, D. D., and Yengo, C. M. (2015) Direct measurements of the coordination of lever arm swing and the catalytic cycle in myosin V. *Proc. Natl. Acad. Sci. U.S.A.* **112**, 14593–14598 [CrossRef Medline](#)
- Muretta, J. M., Rohde, J. A., Johnsrud, D. O., Cornea, S., and Thomas, D. D. (2015) Direct real-time detection of the structural and biochemical events in the myosin power stroke. *Proc. Natl. Acad. Sci. U.S.A.* **112**, 14272–14277 [CrossRef Medline](#)
- Rohde, J. A., Thomas, D. D., and Muretta, J. M. (2017) Heart failure drug changes the mechanoenzymology of the cardiac myosin powerstroke. *Proc. Natl. Acad. Sci. U.S.A.* **114**, E1796–E1804 [CrossRef Medline](#)
- Woody, M. S., Winkelmann, D. A., Capitanio, M., Ostap, E. M., and Goldman, Y. E. (2019) Single molecule mechanics resolves the earliest events in force generation by cardiac myosin. *eLife* **8**, e49266 [CrossRef Medline](#)
- Gunther, L. K., Rohde, J. A., Tang, W., Walton, S. D., Unrath, W. C., Trivedi, D. V., Muretta, J. M., Thomas, D. D., and Yengo, C. M. (2019) Converter domain mutations in myosin alter structural kinetics and motor function. *J. Biol. Chem.* **294**, 1554–1567 [CrossRef Medline](#)
- Kull, F. J., Vale, R. D., and Fletterick, R. J. (1998) The case for a common ancestor: kinesin and myosin motor proteins and G proteins. *J. Muscle Res. Cell Motil.* **19**, 877–886 [CrossRef Medline](#)
- Shimada, T., Sasaki, N., Ohkura, R., and Sutoh, K. (1997) Alanine scanning mutagenesis of the switch I region in the ATPase site of *Dictyostelium discoideum* myosin II. *Biochemistry* **36**, 14037–14043 [CrossRef Medline](#)
- Li, X. D., Rhodes, T. E., Ikebe, R., Kambara, T., White, H. D., and Ikebe, M. (1998) Effects of mutations in the γ -phosphate binding site of myosin on its motor function. *J. Biol. Chem.* **273**, 27404–27411 [CrossRef Medline](#)
- Forgacs, E., Sakamoto, T., Cartwright, S., Belknap, B., Kovács, M., Tóth, J., Webb, M. R., Sellers, J. R., and White, H. D. (2009) Switch 1 mutation

- S217A converts myosin V into a low duty ratio motor. *J. Biol. Chem.* **284**, 2138–2149 [CrossRef Medline](#)
27. Swenson, A. M., Trivedi, D. V., Rauscher, A. A., Wang, Y., Takagi, Y., Palmer, B. M., Málnási-Csizmadia, A., Debold, E. P., and Yengo, C. M. (2014) Magnesium modulates actin binding and ADP release in myosin motors. *J. Biol. Chem.* **289**, 23977–23991 [CrossRef Medline](#)
 28. Trivedi, D. V., David, C., Jacobs, D. J., and Yengo, C. M. (2012) Switch II mutants reveal coupling between the nucleotide- and actin-binding regions in myosin V. *Biophys. J.* **102**, 2545–2555 [CrossRef Medline](#)
 29. Trivedi, D. V., Muretta, J. M., Swenson, A. M., Thomas, D. D., and Yengo, C. M. (2013) Magnesium impacts myosin V motor activity by altering key conformational changes in the mechanochemical cycle. *Biochemistry* **52**, 4710–4722 [CrossRef Medline](#)
 30. Geeves, M. A., Perreault-Micale, C., and Coluccio, L. M. (2000) Kinetic analyses of a truncated mammalian myosin I suggest a novel isomerization event preceding nucleotide binding. *J. Biol. Chem.* **275**, 21624–21630 [CrossRef Medline](#)
 31. Veigel, C., Bartoo, M. L., White, D. C., Sparrow, J. C., and Molloy, J. E. (1998) The stiffness of rabbit skeletal actomyosin cross-bridges determined with an optical tweezers transducer. *Biophys. J.* **75**, 1424–1438 [CrossRef Medline](#)
 32. Neuman, K. C., and Block, S. M. (2004) Optical trapping. *Rev. Sci. Instrum.* **75**, 2787–2809 [CrossRef Medline](#)
 33. Capitanio, M., Canepari, M., Maffei, M., Beneventi, D., Monico, C., Vanzi, F., Bottinelli, R., and Pavone, F. S. (2012) Ultrafast force-clamp spectroscopy of single molecules reveals load dependence of myosin working stroke. *Nat. Methods* **9**, 1013–1019 [CrossRef Medline](#)
 34. Fischer, S., Windshügel, B., Horak, D., Holmes, K. C., and Smith, J. C. (2005) Structural mechanism of the recovery stroke in the myosin molecular motor. *Proc. Natl. Acad. Sci. U.S.A.* **102**, 6873–6878 [CrossRef Medline](#)
 35. Kiani, F. A., and Fischer, S. (2016) ATP-dependent interplay between local and global conformational changes in the myosin motor. *Cytoskeleton (Hoboken)* **73**, 643–651 [CrossRef Medline](#)
 36. Nsemelov, Y. E., Agafonov, R. V., Negrashov, I. V., Blakely, S. E., Titus, M. A., and Thomas, D. D. (2011) Structural kinetics of myosin by transient time-resolved FRET. *Proc. Natl. Acad. Sci. U.S.A.* **108**, 1891–1896 [CrossRef Medline](#)
 37. Málnási-Csizmadia, A., Pearson, D. S., Kovács, M., Woolley, R. J., Geeves, M. A., and Bagshaw, C. R. (2001) Kinetic resolution of a conformational transition and the ATP hydrolysis step using relaxation methods with a *Dictyostelium* myosin II mutant containing a single tryptophan residue. *Biochemistry* **40**, 12727–12737 [CrossRef Medline](#)
 38. Yengo, C. M., and Sweeney, H. L. (2004) Functional role of loop 2 in myosin V. *Biochemistry* **43**, 2605–2612 [CrossRef Medline](#)
 39. Joel, P. B., Sweeney, H. L., and Trybus, K. M. (2003) Addition of lysines to the 50/20 kDa junction of myosin strengthens weak binding to actin without affecting the maximum ATPase activity. *Biochemistry* **42**, 9160–9166 [CrossRef Medline](#)
 40. Kintsés, B., Gyimesi, M., Pearson, D. S., Geeves, M. A., Zeng, W., Bagshaw, C. R., and Málnási-Csizmadia, A. (2007) Reversible movement of switch 1 loop of myosin determines actin interaction. *EMBO J.* **26**, 265–274 [CrossRef Medline](#)
 41. Reubold, T. F., Eschenburg, S., Becker, A., Kull, F. J., and Manstein, D. J. (2003) A structural model for actin-induced nucleotide release in myosin. *Nat. Struct. Biol.* **10**, 826–830 [CrossRef Medline](#)
 42. Preller, M., and Manstein, D. J. (2013) Myosin structure, allostery, and mechano-chemistry. *Structure* **21**, 1911–1922 [CrossRef Medline](#)
 43. Houdusse, A., and Sweeney, H. L. (2016) How myosin generates force on actin filaments. *Trends Biochem. Sci.* **41**, 989–997 [CrossRef Medline](#)
 44. Sun, M., Rose, M. B., Ananthanarayanan, S. K., Jacobs, D. J., and Yengo, C. M. (2008) Characterization of the pre-force-generation state in the actomyosin cross-bridge cycle. *Proc. Natl. Acad. Sci. U.S.A.* **105**, 8631–8636 [CrossRef Medline](#)
 45. Dantzig, J. A., Goldman, Y. E., Millar, N. C., Laktis, J., and Homsher, E. (1992) Reversal of the cross-bridge force-generating transition by photo-generation of phosphate in rabbit psoas muscle fibres. *J. Physiol.* **451**, 247–278 [CrossRef Medline](#)
 46. Walker, J. W., Lu, Z., and Moss, R. L. (1992) Effects of Ca²⁺ on the kinetics of phosphate release in skeletal muscle. *J. Biol. Chem.* **267**, 2459–2466 [Medline](#)
 47. Debold, E. P., Turner, M. A., Stout, J. C., and Walcott, S. (2011) Phosphate enhances myosin-powered actin filament velocity under acidic conditions in a motility assay. *Am. J. Physiol. Regul. Integr. Comp. Physiol.* **300**, R1401–R1408 [CrossRef Medline](#)
 48. Debold, E. P., Walcott, S., Woodward, M., and Turner, M. A. (2013) Direct observation of phosphate inhibiting the force-generating capacity of a miniensemble of myosin molecules. *Biophys. J.* **105**, 2374–2384 [CrossRef Medline](#)
 49. Caremani, M., Melli, L., Dolfi, M., Lombardi, V., and Linari, M. (2015) Force and number of myosin motors during muscle shortening and the coupling with the release of the ATP hydrolysis products. *J. Physiol.* **593**, 3313–3332 [CrossRef Medline](#)
 50. Caremani, M., Melli, L., Dolfi, M., Lombardi, V., and Linari, M. (2013) The working stroke of the myosin II motor in muscle is not tightly coupled to release of orthophosphate from its active site. *J. Physiol.* **591**, 5187–5205 [CrossRef Medline](#)
 51. De La Cruz, E. M., Wells, A. L., Rosenfeld, S. S., Ostap, E. M., and Sweeney, H. L. (1999) The kinetic mechanism of myosin V. *Proc. Natl. Acad. Sci. U.S.A.* **96**, 13726–13731 [CrossRef Medline](#)
 52. Mehta, A. D., Rock, R. S., Rief, M., Spudich, J. A., Mooseker, M. S., and Cheney, R. E. (1999) Myosin-V is a processive actin-based motor. *Nature* **400**, 590–593 [CrossRef Medline](#)
 53. De La Cruz, E. M., and Ostap, E. M. (2004) Relating biochemistry and function in the myosin superfamily. *Curr. Opin. Cell Biol.* **16**, 61–67 [CrossRef Medline](#)
 54. Yengo, C. M., De la Cruz, E. M., Safer, D., Ostap, E. M., and Sweeney, H. L. (2002) Kinetic characterization of the weak binding states of myosin V. *Biochemistry* **41**, 8508–8517 [CrossRef Medline](#)
 55. Joel, P. B., Trybus, K. M., and Sweeney, H. L. (2001) Two conserved lysines at the 50/20-kDa junction of myosin are necessary for triggering actin activation. *J. Biol. Chem.* **276**, 2998–3003 [CrossRef Medline](#)
 56. Várkuti, B. H., Yang, Z., Kintsés, B., Erdélyi, P., Bardos-Nagy, I., Kovacs, A. L., Hári, P., Kellermayer, M., Vellai, T., and Málnási-Csizmadia, A. (2012) A novel actin binding site of myosin required for effective muscle contraction. *Nat. Struct. Mol. Biol.* **19**, 299–306 [CrossRef Medline](#)
 57. Murphy, C. T., and Spudich, J. A. (2000) Variable surface loops and myosin activity: accessories to a motor. *J. Muscle Res. Cell Motil.* **21**, 139–151 [CrossRef Medline](#)
 58. Chalovich, J. M., and Eisenberg, E. (1982) Inhibition of actomyosin ATPase activity by troponin-tropomyosin without blocking the binding of myosin to actin. *J. Biol. Chem.* **257**, 2432–2437 [Medline Medline](#)
 59. Trybus, K. M., and Taylor, E. W. (1980) Kinetic studies of the cooperative binding of subfragment 1 to regulated actin. *Proc. Natl. Acad. Sci. U.S.A.* **77**, 7209–7213 [CrossRef Medline](#)
 60. McKillop, D. F., and Geeves, M. A. (1991) Regulation of the acto.myosin subfragment 1 interaction by troponin/tropomyosin: evidence for control of a specific isomerization between two acto.myosin subfragment 1 states. *Biochem. J.* **279**, 711–718 [CrossRef Medline](#)
 61. White, H. D., Belknap, B., and Webb, M. R. (1997) Kinetics of nucleoside triphosphate cleavage and phosphate release steps by associated rabbit skeletal actomyosin, measured using a novel fluorescent probe for phosphate. *Biochemistry* **36**, 11828–11836 [CrossRef Medline](#)
 62. Pardee, J. D., and Spudich, J. A. (1982) Purification of muscle actin. *Methods Enzymol.* **85**, 164–181 [CrossRef Medline](#)
 63. Criddle, A. H., Geeves, M. A., and Jeffries, T. (1985) The use of actin labelled with *N*-(1-pyrenyl)iodoacetamide to study the interaction of actin with myosin subfragments and troponin/tropomyosin. *Biochem. J.* **232**, 343–349 [CrossRef Medline](#)
 64. De La Cruz, E. M., and Ostap, E. M. (2009) Kinetic and equilibrium analysis of the myosin ATPase. *Methods Enzymol.* **455**, 157–192 [CrossRef Medline](#)
 65. Muretta, J. M., Petersen, K. J., and Thomas, D. D. (2013) Direct real-time detection of the actin-activated power stroke within the myosin catalytic domain. *Proc. Natl. Acad. Sci. U.S.A.* **110**, 7211–7216 [CrossRef Medline](#)

66. Unger, M., and Debold, E. P. (2019) Acidosis decreases the Ca^{2+} sensitivity of thin filaments by preventing the first actomyosin interaction. *Am. J. Physiol. Cell Physiol.* **317**, C714–C718 [CrossRef](#) [Medline](#)
67. Smith, D. A., Steffen, W., Simmons, R. M., and Sleep, J. (2001) Hidden-Markov methods for the analysis of single-molecule actomyosin displacement data: the variance-hidden-Markov method. *Biophys. J.* **81**, 2795–2816 [CrossRef](#) [Medline](#)
68. Beausang, J. F., Goldman, Y. E., and Nelson, P. C. (2011) Change-point analysis for single-molecule polarized total internal reflection fluorescence microscopy experiments. *Methods Enzymol.* **487**, 431–463 [CrossRef](#) [Medline](#)
69. Veigel, C., Molloy, J. E., Schmitz, S., and Kendrick-Jones, J. (2003) Load-dependent kinetics of force production by smooth muscle myosin measured with optical tweezers. *Nat. Cell Biol.* **5**, 980–986 [CrossRef](#) [Medline](#)
70. Visser, I., and Speekenbrink, M. (2010) depmixS4: an R package for hidden Markov models. *J. Stat. Softw.* **36**, 1–21 [CrossRef](#)

FRET and optical trapping reveal mechanisms of actin activation of the power stroke and phosphate release in myosin V

Laura K. Gunther, John A. Rohde, Wanjian Tang, Joseph A. Cirilo Jr., Christopher P. Marang, Brent D. Scott, David D. Thomas, Edward P. Debold and Christopher M. Yengo

J. Biol. Chem. 2020, 295:17383-17397.

doi: 10.1074/jbc.RA120.015632 originally published online October 14, 2020

Access the most updated version of this article at doi: [10.1074/jbc.RA120.015632](https://doi.org/10.1074/jbc.RA120.015632)

Alerts:

- [When this article is cited](#)
- [When a correction for this article is posted](#)

[Click here](#) to choose from all of JBC's e-mail alerts

This article cites 70 references, 22 of which can be accessed free at <http://www.jbc.org/content/295/51/17383.full.html#ref-list-1>

Supporting Information for

**FRET and optical trapping reveal mechanisms of actin-activation of the
power stroke and phosphate-release in myosin V**

By Laura K. Gunther et al.

This PDF file contains:

Supporting Tables S1-3

Supporting Figures S1-9

SI Materials and Methods.

Table S1. Rate constants used for simulations.

Rate Constant (s ⁻¹)	WT	S217A
k'_{+1T}	2	1
k'_{-1T}	1000	1000
k'_{+2T}	1000	400
k'_{-2T}	0.001	0.001
$k_{+Dissoc}$	10	10
$k_{-Dissoc}$	1000	1000
k_{+H}	320	8
k_{-H}	80	2
k_{+Assoc}	*50 or 85.5	*1.6 or 3.6
k_{-Assoc}	1000	1000
k'_{+PWF}	410	410
k'_{-PWF}	1	1
k'_{+Pi}	500	500
k'_{-Pi}	1	1
k'_{+PWS}	80	40
k'_{-PWS}	20	80
$k'_{+D'}$	50	50
$k'_{-D'}$	5	5
k'_{+D}	24	46
k'_{-D}	1	1

*Rate constant was only used for ATPase simulations.

Table S2. Transient time-resolved donor-only fluorescence parameters.

Construct	Amplitudes		Lifetimes	
	A ₁ (fraction)	A ₂ (fraction)	τ ₁ (ns)	τ ₂ (ns)
WT & S217A	0.61	0.39	4.68	0.51

The data sets for both WT and S217A were globally fit to a two exponential lifetime decay. No changes in the donor-only fluorescence lifetimes were observed when comparing WT and S217A. When WT and S217A were fit separately the time resolved lifetime parameters were not statistically different. $\chi^2 = 0.82$ for the globally fit model.

Table S3. Summary of optical trapping results.

^aOptical trapping (\pmSE)	WT n=352	S217A n=428
Unitary displacement (nm)	3.0 \pm 0.4	*4.9 \pm 0.4
Attached time (ms)	231 \pm 39	*112 \pm 17
^bEnsemble averaging of positive displacements (\pmSE)		
Working stroke rate constant (s ⁻¹)	629 \pm 16	*867 \pm 33
Unitary displacement (nm)	6.9 \pm 0.1	6.6 \pm 0.1
Event frequency (\pmSE)		
Average event frequency per experiment (events/sec)	0.42 \pm 0.10	0.60 \pm 0.15

^aSee Figure S8

^bSee Figure 6

^cSee Figure S9

* $p < 0.01$

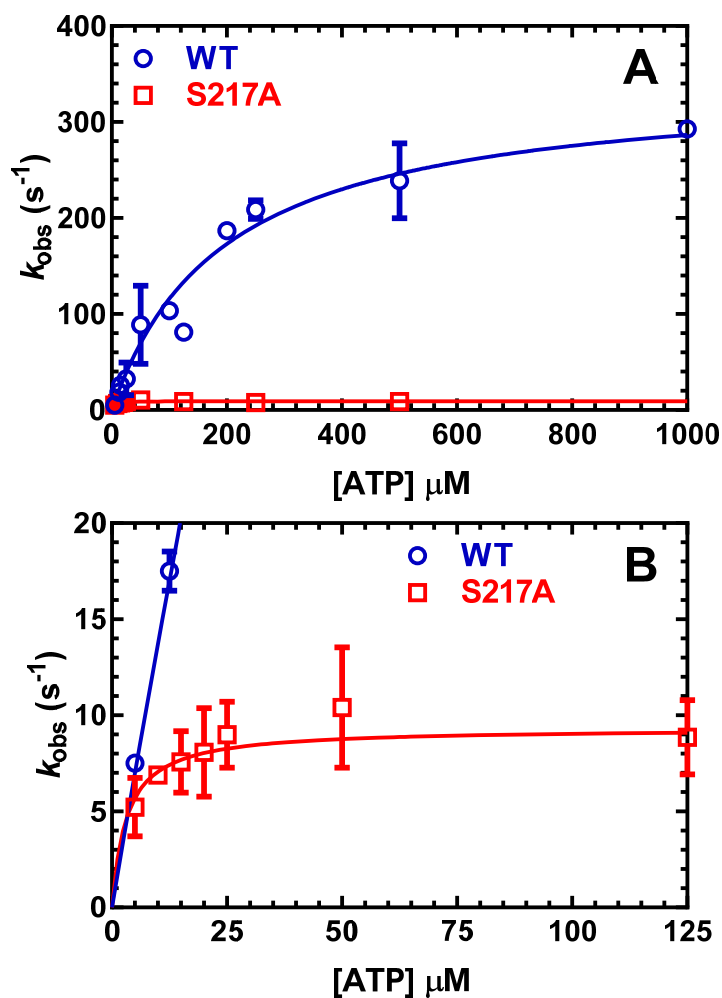


Figure S1. ATP binding and hydrolysis. The intrinsic tryptophan fluorescence enhancement observed upon ATP binding to WT or S217A MV was used to monitor ATP binding and hydrolysis. MV was mixed with varying concentrations of ATP and the fluorescence transients were fit to a single exponential function. The observed rate constants were plot as a function of ATP concentration to determine the maximum rate of ATP hydrolysis (k_{+H+H}) and second-order rate constant for ATP binding ($K_{1T}k_{+2T}$).

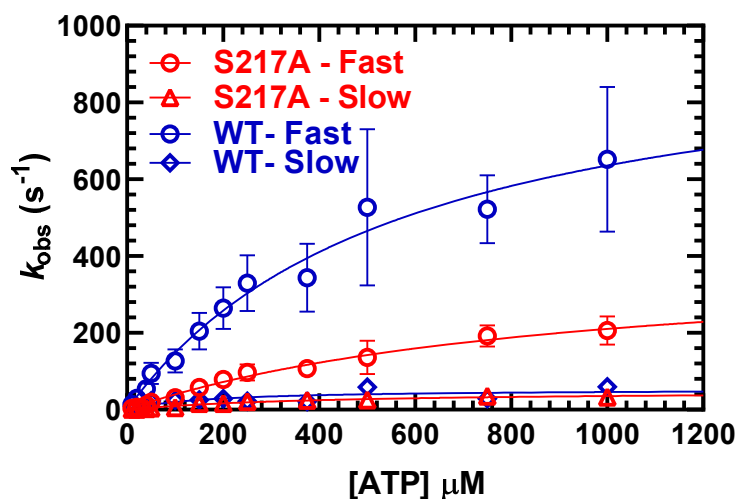


Figure S2. ATP-induced dissociation from pyrene actin. The ATP-induced transition into the weak actin binding states was monitored by mixing a complex of pyrene acto-MV with varying concentration of ATP. The pyrene fluorescence increase observed upon population of the weak actin binding states was best fit by a two exponential function at each ATP concentration. The observed fast and slow phases were hyperbolically dependent on ATP concentration. The fast phase was 90% and 70% of the fluorescence signal in WT and S217A, respectively. The fast phase was used to determine the maximum rate of ATP-induced dissociation (k'_{+2T}) and the second order rate constant for ATP binding to acto-MV ($K'_{1T}k'_{+2T}$).

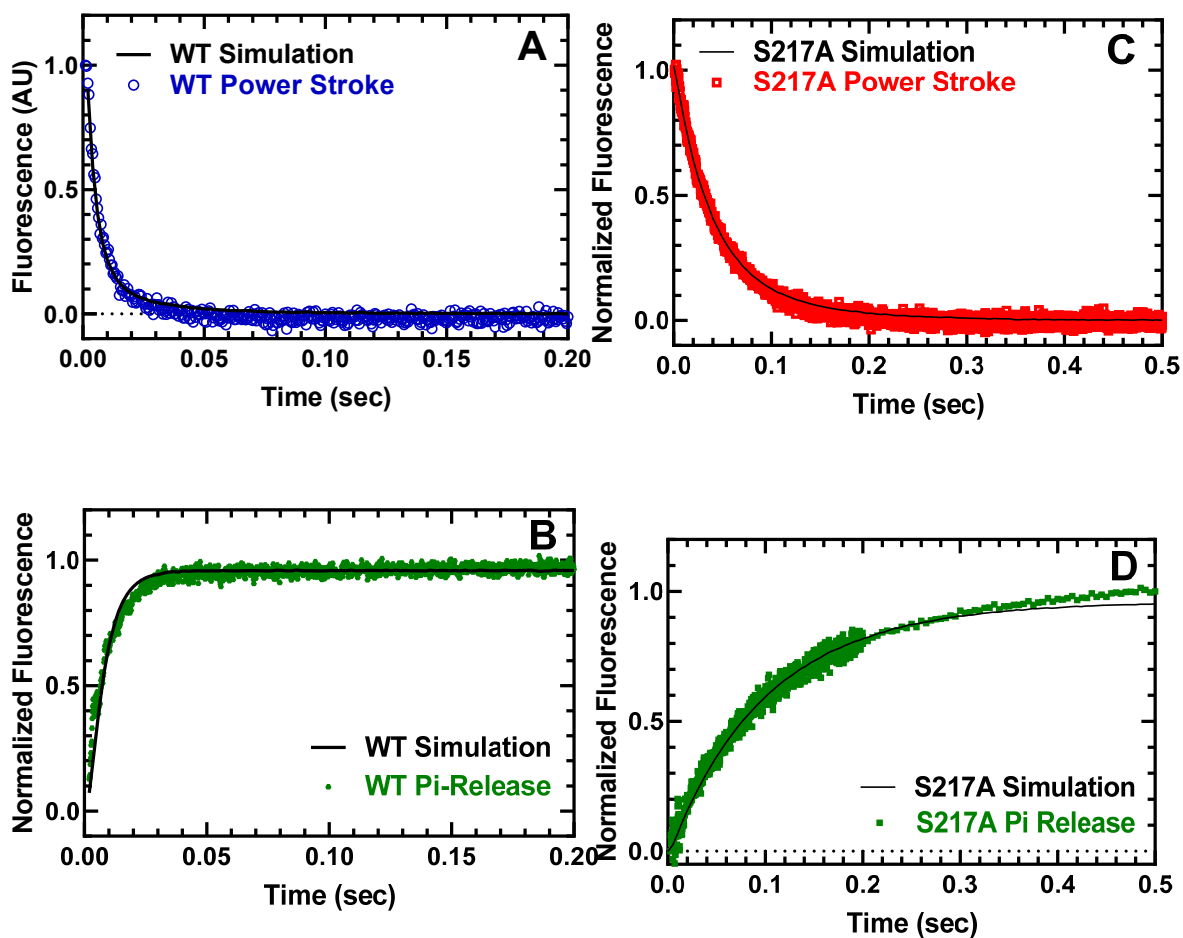


Figure S3. Simulations of power stroke and phosphate release transients. The power stroke fluorescence transients acquired at 30 μM actin are compared to simulations generated using the proposed kinetic model (rate constants are in Table S2) for (A) WT and (C) S217A. The phosphate-release fluorescence transients at 10 μM actin are compared to simulations generated using the proposed kinetic model (rate constants are in Table S1) for (B) WT and (D) S217A.

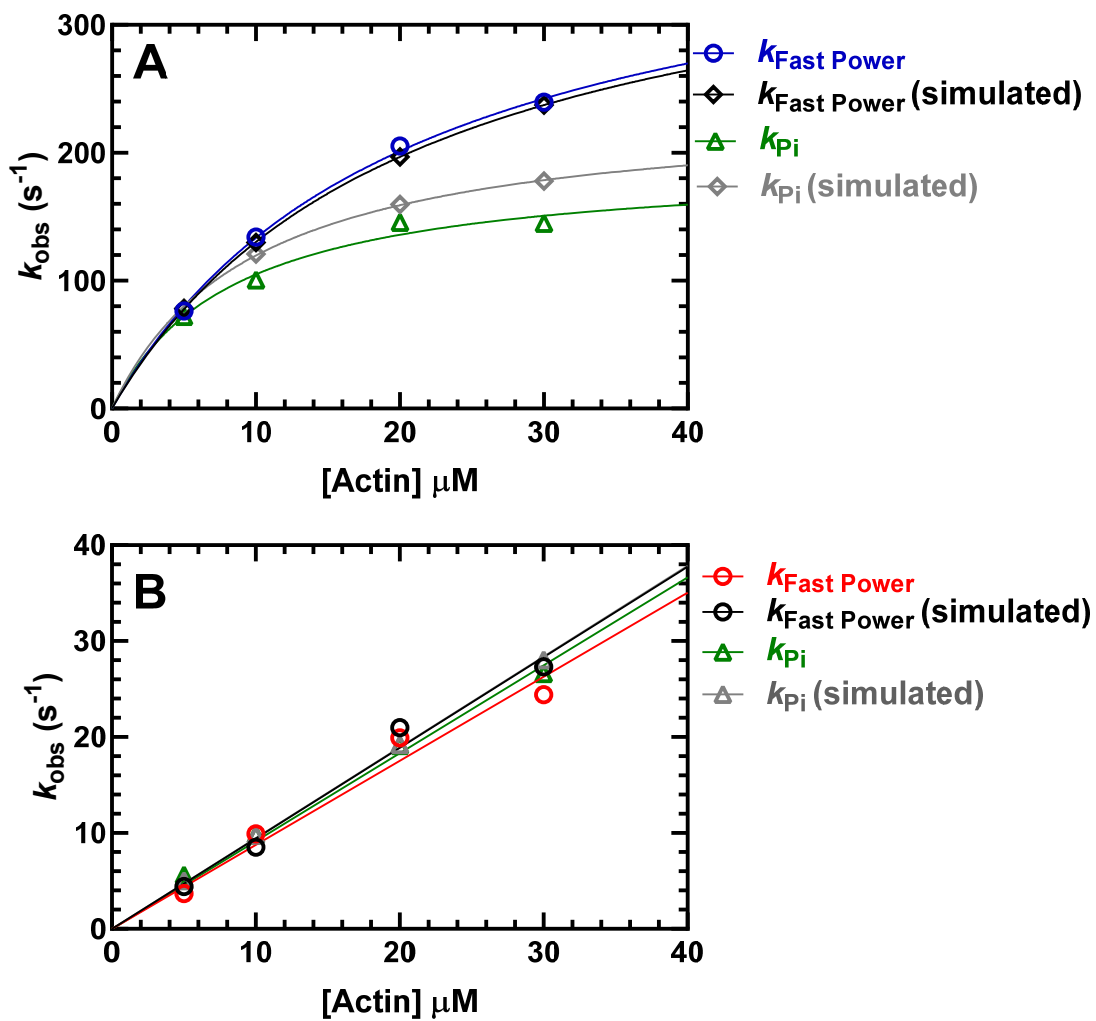


Figure S4. Simulated data sets of the power stroke and phosphate release. Synthetic data was generated using the proposed kinetic model and conditions used experimentally. The data were fit to the appropriate exponential function. The rate constants of the fast power stroke ($k_{\text{Fast Power}}$) and phosphate release (k_{Pi}) are shown in comparison to the experimental data for A) WT and B) S217A.

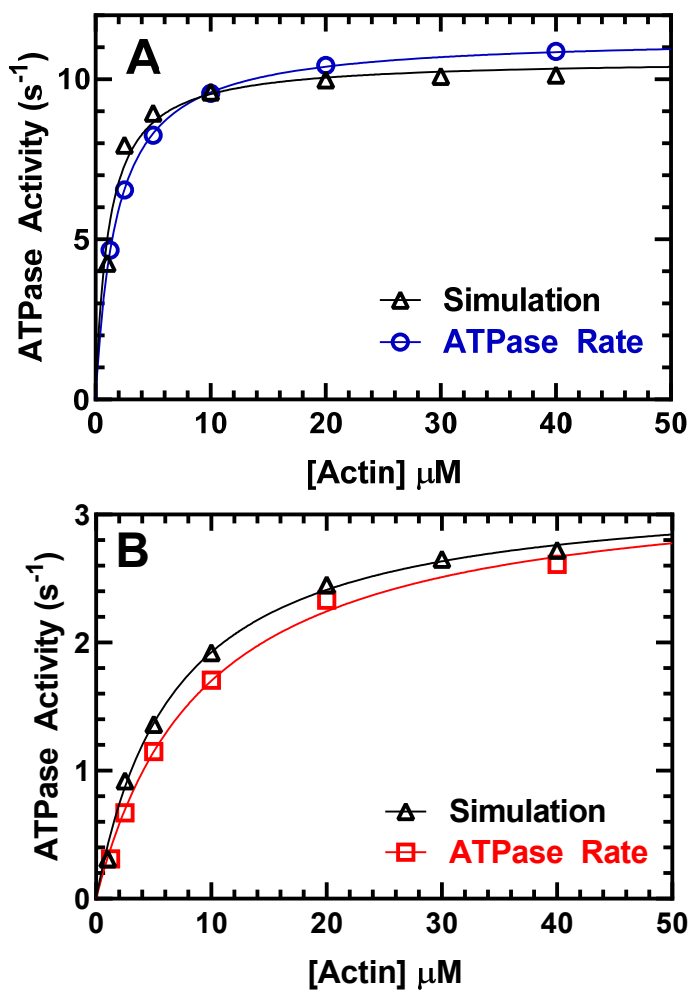


Figure S5. Simulations of actin-activated ATPase. The proposed kinetic model was evaluated by producing simulated actin-activated ATPase data using the rate constants shown in Table S1. The simulated and experimental data are compared for A) WT and B) S217A.

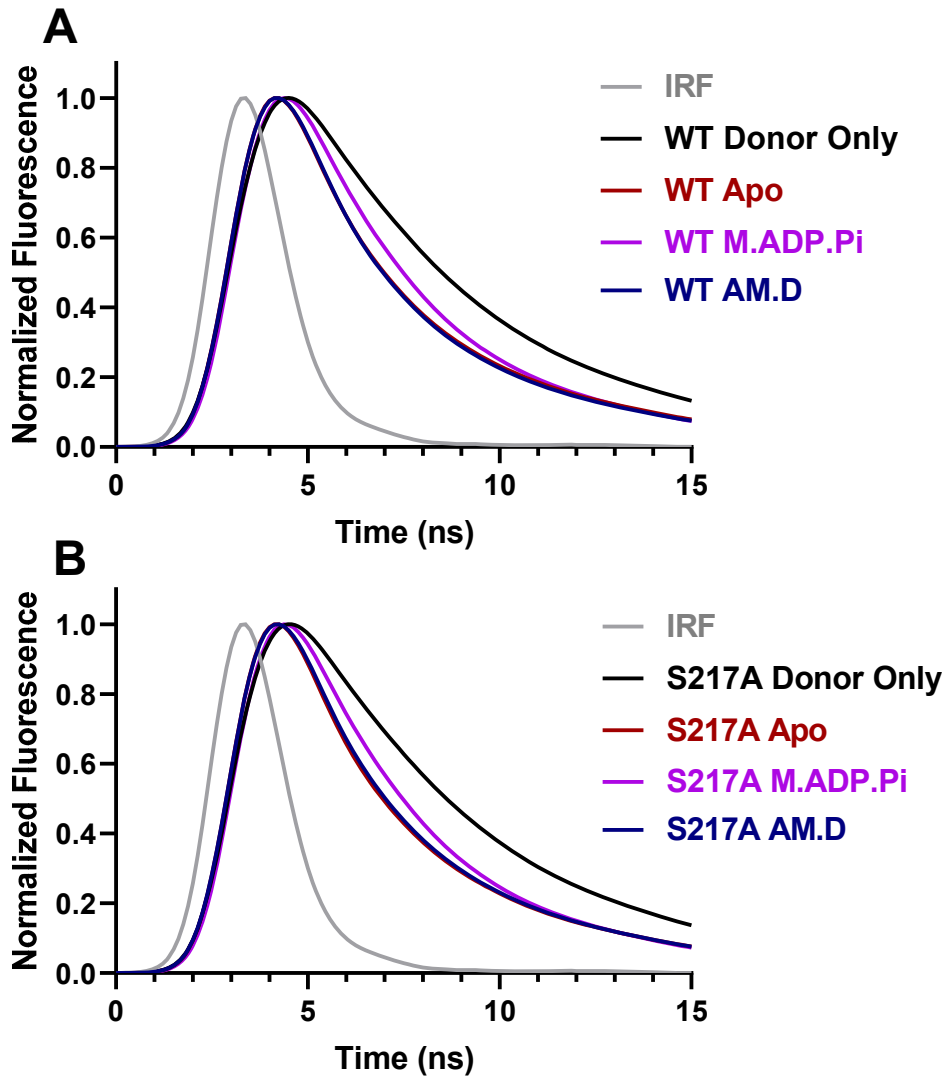


Figure S6. Fluorescence waveforms detection time-resolved FRET in different conditions. Time-resolved FRET measurements acquired under equilibrium or steady-state ATPase cycling biochemical conditions for A) WT and B) S217A. The instrument response function (IRF), or detected laser pulse, is shown in gray. Time-resolved fluorescence decays of FRET labeled MV samples (160 nM MV FAsH.QSY-CaM (Donor + Acceptor, D+A)) in three biochemical states: Apo (brown), with 20 μ M Actin and 4.0 mM ADP (navy), or with 4.0 mM ATP (magenta). The donor only fluorescence of 160 nM MV FAsH is shown for comparison (black)

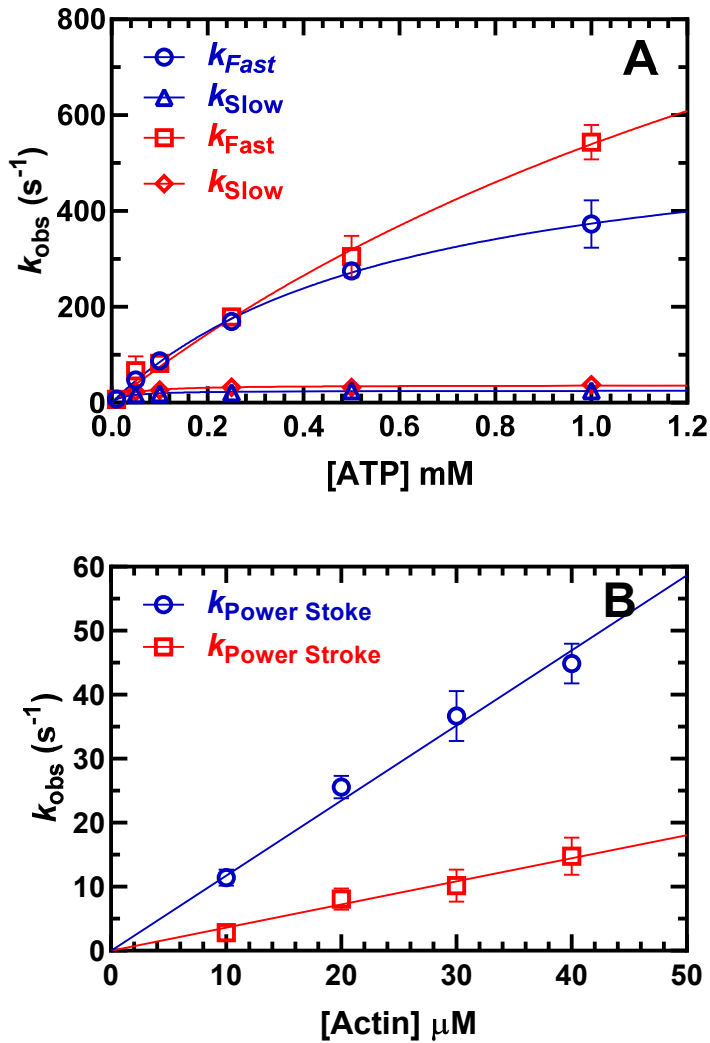


Figure S7. Transient time-resolved FRET (TR²FRET): time-resolved fluorescence waveform acquisition of structural kinetics. A) Summary of rate constants from fitting the recovery-stroke TR²FRET data. The fluorescence of 160 nM MV FIAsh.QSY-CaM changes upon rapid stopped-flow mixing with varying concentrations of ATP and data were best fit to a two-exponential function. The hyperbolic fit of the data allowed determination of the maximum rate of the fast and slow recovery stroke rate constant (WT = 601 ± 17 and 25 ± 1 s⁻¹; S217A = 1732 ± 436 and 37 ± 2 s⁻¹, respectively). B) Summary of rate constants from fitting the power-stroke TR²FRET. 160 nM MV and 10 μM ATP were mixed with 5.0 mM ADP and varying actin concentrations. Data were fit to a single exponential function and rate constants plot as a function of actin concentration were fit to a linear relationship for both WT and S217A (slope = 1.17 ± 0.04 and 0.36 ± 0.01 μM⁻¹·s⁻¹, respectively) thus likely represents an ensemble of both the fast and slow power stroke rate constants measured by sequential mix stopped-flow FRET (see Figure 3)

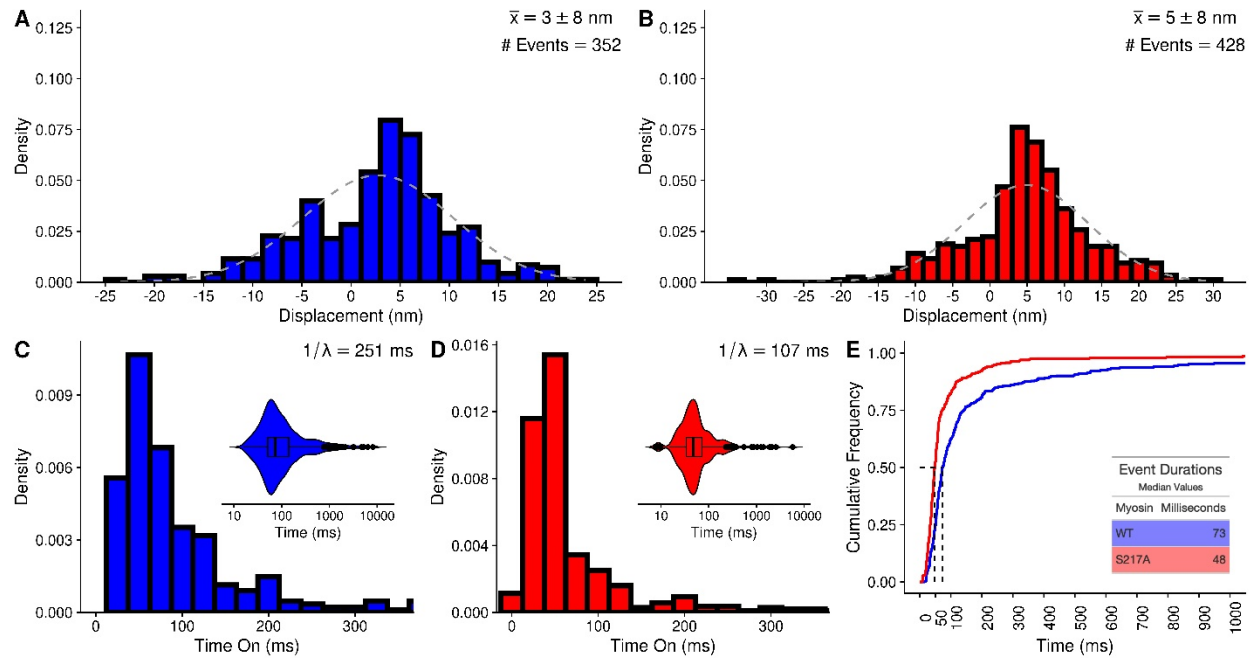


Figure S8. Single molecule optical trapping data distributions. Histograms of binding event displacements for A) WT (blue) and B) S217A (red) fit with a Gaussian curve with the mean \pm SD shown in the insets. Distributions of event lifetimes for C) WT and D) S217A, fit to a single exponential decay with average event lifetime ($1/\lambda$) shown in the insets. Events were detected using a Hidden-Markov analysis and the start and end of each event was determined using change-point analysis (see Methods). Representative raw displacement records are show in the main text (see Figure 6). See Table S3 for summary and statistical analysis. E) Event lifetime data replotted as cumulative distributions with the median values indicated for the WT (red) and S217A (blue).

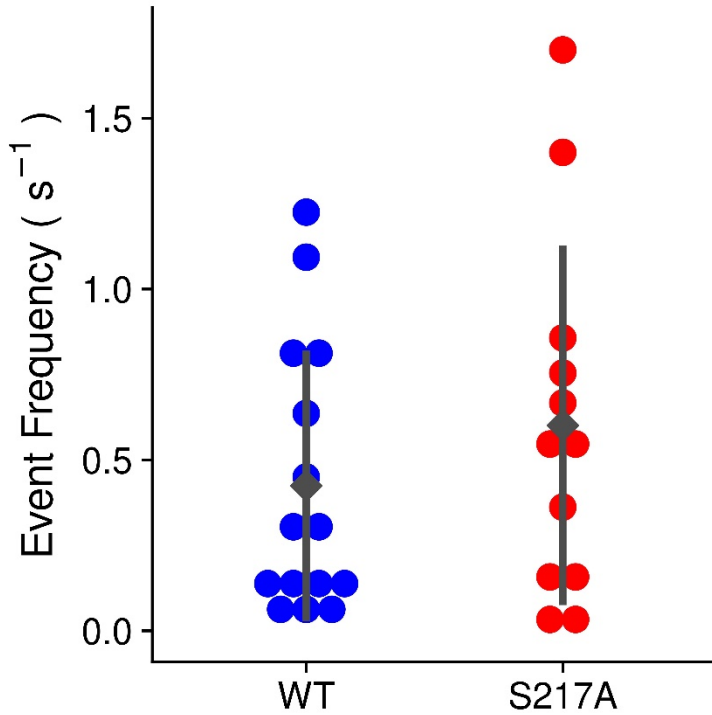


Figure S9. Event frequencies for optical trapping data. Each data represents a recording of data over a period of time ranging from 30sec to 2min. Within each recording the event frequency was determined as the number of events divided by the duration of the recording. Grey diamond and error bars represent the mean and SD. The Mean and SEM are 0.424 ± 0.102 for WT and 0.601 ± 0.0152 for S217A. The number of records were $n=15$ and $n=12$ for WT and S217A, respectively. Significance was tested using a Welch Two Sample t test ($p = 0.3447$). See Table S3 for summary.